

Fickian yet non-Gaussian diffusion in an annealed heterogeneous environment

Seongyu Park,¹ Xavier Durang,¹ Ralf Metzler,^{2,3} and Jae-Hyung Jeon^{1,3,4,*}

¹*Department of Physics, Pohang University of Science and Technology (POSTECH), Pohang 37673, Republic of Korea*

²*Institute of Physics & Astronomy, University of Potsdam, 14476 Potsdam-Golm, Germany*

³*Asia Pacific Center for Theoretical Physics (APCTP), Pohang 37673, Republic of Korea*[†]

⁴*School of Physics, Korea Institute for Advanced Study (KIAS), Seoul 130-722, Republic of Korea*

(Dated: March 20, 2025)

Fickian yet non-Gaussian diffusion is a ubiquitous phenomenon observed in various biological and soft matter systems. This anomalous dynamics is typically attributed to heterogeneous environments inducing spatiotemporal variations in the diffusivity of tracer particles. While previous studies have predominantly focused on systems exhibiting either spatial or temporal heterogeneity, this work bridges the gap by introducing a model based on an annealed extreme landscape to simultaneously account for both types of heterogeneities. Through a combination of computational analyses and analytical derivations, we investigate how the interplay of spatial and temporal heterogeneities in the energy landscape gives rise to Fickian yet non-Gaussian diffusion. Furthermore, we demonstrate that in the presence of temporal environmental fluctuations, the heterogeneous diffusion inevitably converges to classical Brownian motion via a homogenization process. We derive an analytical expression for the homogenization time as a function of key parameters governing the system's spatiotemporal heterogeneities. Additionally, we quantify particle-to-particle diffusion heterogeneity and examine the ergodic properties of this model, providing deeper insights into the dynamics of complex, heterogeneous systems.

I. INTRODUCTION

Diffusion is a fundamental process that underpins various cellular and biological phenomena. For instance, it plays a critical role in molecular mechanisms such as the transcription and translation of DNA sequences [1–4], cellular signaling mediated by membrane proteins [5], the transport of mRNA–protein complexes [6–8], as well as cellular motion and the transport of cargo on cell carpets at longer times [9–11]. Recent advances in microscopy and single-particle tracking techniques have enabled in-depth studies into the diffusion dynamics of a wide range of biological tracers. These studies have revealed that diffusion in biological systems often deviates from the classical Brownian motion paradigm [12–15]. Notably, anomalous diffusion—characterized by a power-law scaling of the mean squared displacement (MSD) with time of the form $\langle x(t)^2 \rangle \propto t^\alpha$ with $\alpha \neq 1$ —has emerged as a hallmark in these systems [13, 16, 17]. Subdiffusion with $0 < \alpha < 1$ is typically attributed to environmental factors such as macromolecular crowding, viscoelastic properties of the medium, or transient trapping induced by power-law, scale-free waiting times [18–20].

More recently, research has shifted focus toward a distinct phenomenon known as Fickian yet non-Gaussian diffusion. This behavior, observed in diverse soft and biological matter systems, is characterized by normal diffusion (linear MSD scaling with time) but a substantial deviation from the Gaussian probability density function (PDF) of the displacements [21–27]. Instead, these

systems exhibit non-Gaussian PDFs, often resembling Laplace distributions of the form

$$p(x, t) \propto \exp(-|x|/\lambda(t)), \quad (1)$$

with the time-dependent width $\lambda(t)$ that may scale as $\lambda(t) \simeq t^{1/2}$ or $\simeq t^{1/3}$ [28, 29]. Additional power-law corrections may modify the Laplace shape, especially around the cusp [21, 28, 30]. The origin of this non-Gaussianity is typically attributed to environmental heterogeneities [5, 22, 26, 28, 30–34] or the conformational variability of the tracer particles [35–38]. In many cases, fluctuations in particle diffusivity are described by a static distribution of diffusivity values, $\psi(D)$, leading to the superstatistical formulation for the PDF [39]

$$p(x, t) = \int_0^\infty dD \psi(D) G(x, t|D), \quad (2)$$

where $G(x, t|D) = (4\pi Dt)^{-1/2} \exp(-x^2/[4Dt])$ is a Gaussian propagator for a given diffusivity D . Certain formulations of diffusing-diffusivity models have the superstatistical formulation as their short-time limit, see, e.g., [28, 30].

The description of fluctuating diffusivities varies with the temporal and spatial characteristics of the system. For environments with rapid temporal fluctuations relative to the particle dynamics, the diffusivity can be treated as a stochastic, exclusively time-dependent variable $D(t)$ [28, 30–32, 34, 40], which in the area of stochastic processes is often referred to as *annealed disorder* [41, 42]. A prominent example of the annealed disorder is the diffusing diffusivity model suggested by Chubynsky and Slater [31], which was further elaborated by Chechkin *et al* [28]. Conversely, for systems with slow environmental changes, diffusivity is better represented

*jeonjh@postech.ac.kr

[†]rmetzler@uni-potsdam.de

as a spatially dependent variable $D(\mathbf{r})$ [43–45], which is called *quenched disorder* [41, 42]. In quenched systems, typically, the diffusivity has the same value each time the particle (re)visits the same location in space, leading to the buildup of correlations.

However, many biological systems exhibit more complex spatiotemporal heterogeneities, where neither annealed nor quenched disorder alone suffices to adequately describe the observed diffusive dynamics. Examples include crowded cellular membranes [5, 46–48], dynamic chromatin structures [49–57], crowded polydisperse vacuole systems [58, 59], and active cytoskeletal networks [57, 60–63].

In this study, we explore the Fickian yet non-Gaussian diffusion of tracer particles in a novel spatiotemporally heterogeneous medium, the *annealed extreme landscape*. This framework integrates both spatial and temporal dependencies of diffusivity, capturing the intricate interplay between environmental heterogeneity and particle dynamics. By combining analytic derivations and computational simulations, we investigate key diffusion metrics, including MSDs, Van-Hove self-correlation functions, non-Gaussianity, and ergodicity breaking parameters. Our analysis elucidates how these quantities evolve with varying environmental fluctuation scales and reveals the homogenization process as a consequence of which non-Gaussian diffusion eventually cross over to Gaussian behavior. Through these investigations, we aim to provide a comprehensive understanding of diffusion dynamics in complex, heterogeneous media.

This work is organized as follows. Section II introduces the annealed extreme landscape model, outlining several dynamic observables used to quantify the spatiotemporal heterogeneity of the energy landscape. In Sec. III, we investigate the diffusion dynamics in the annealed extreme landscape, focusing on quantities such as MSD, the Van-Hove self-correlation function, and measures of non-Gaussianity. Furthermore, we observe the Fickian yet non-Gaussian diffusion and provide an analytical framework to explain this effect under quenched and fast-annealing conditions. Section IV delves into the homogenization process, deriving the analytic expression for the homogenization time based on the self-similarity of the random energy landscape. Additionally, we explore particle-to-particle diffusion heterogeneity via the ergodicity-breaking parameter. Finally, Sec. V concludes by summarizing the key findings and discussing their implications for the understanding of Fickian yet non-Gaussian diffusion phenomena.

II. ANNEALED EXTREME LANDSCAPE MODEL

In this Section, we model the spatiotemporal heterogeneous diffusion of tracers embedded in an environment whose randomness changes over time. We describe such random media using a two-dimensional lattice model

called the annealed extreme landscape. Here, we encapsulate the essence of this model along with the introduction of associated dynamic observables we developed, which are called the local diffusivity field (Sec. II B) and the sampled diffusivity (Sec. II C).

A. Annealed extreme landscape

We extend the quenched extreme landscape model introduced in Refs. [44, 45] to incorporate temporal fluctuations. The annealed extreme landscape is constructed by the following steps:

(i) *Auxiliary random field*. First, consider a two-dimensional square lattice of size $L \times L$ with the lattice constant $a = 1$. Every lattice point $\mathbf{r} = (x, y)$ is allocated the auxiliary random energy $U(\mathbf{r})$, drawn from the exponential PDF [Fig. 1(a)]

$$\phi_U[U(\mathbf{r}) = U] = U_0^{-1} \exp\left(-\frac{U}{U_0}\right), \quad U < 0. \quad (3)$$

We refer to the set of random variables $\{U(\mathbf{r})\}$ as an auxiliary random field. In our study, we set the parameter U_0 to unity for simplicity and typically consider a random field of size $L = 512$, unless specified otherwise.

(ii) *Extreme landscape*. Once the auxiliary random field $U(\mathbf{r})$ is given, the extreme landscape $V(\mathbf{r})$ is defined at each lattice point \mathbf{r} as the local minimum value among the neighboring values $U(\mathbf{r}')$ within a critical radius r_c (as shown in the middle panel of Fig. 1(a)). This is mathematically expressed as

$$V(\mathbf{r}) = \min[U(\mathbf{r}') \mid \|\mathbf{r} - \mathbf{r}'\| \leq r_c]. \quad (4)$$

In a finite lattice space, periodic boundary conditions are employed to construct $V(\mathbf{r})$. When r_c is sufficiently large, the distribution of $V(\mathbf{r})$ is known to obey the Gumbel distribution [44, 45]

$$\phi_V[V(\mathbf{r}) = V] \approx \exp\left[V - V_0 - \exp(V - V_0)\right] \quad (5)$$

where $V < 0$ and $V_0 = -\log(\pi r_c^2/a^2)$. Throughout our work, we set the critical radius to be $r_c = 10$ in our simulations. The right panel of Fig. 1(a) illustrates an example of the computer-generated extreme landscape.

(iii) *Annealing*. For a given time interval δ , we randomly choose $L^2 \omega_{\text{env}} \delta/2$ lattice points (where ω_{env} is the annealing rate per unit time $t_0 (= 1)$) and update their auxiliary random fields according to the following rule: For a chosen lattice point \mathbf{r} and one of its four nearest neighbors \mathbf{r}' , we exchange their respective random fields $U(\mathbf{r})$ and $U(\mathbf{r}')$ with each other. Note that ω_{env} can be interpreted as the average number of exchange events per lattice point per unit time. For a more detailed description of the algorithm, we refer to App. A.

(iv) Repeat the above processes (ii) and (iii) every time interval δ to realize the annealed extreme landscape $V(\mathbf{r}, t)$, that then becomes a fluctuating field over time t .

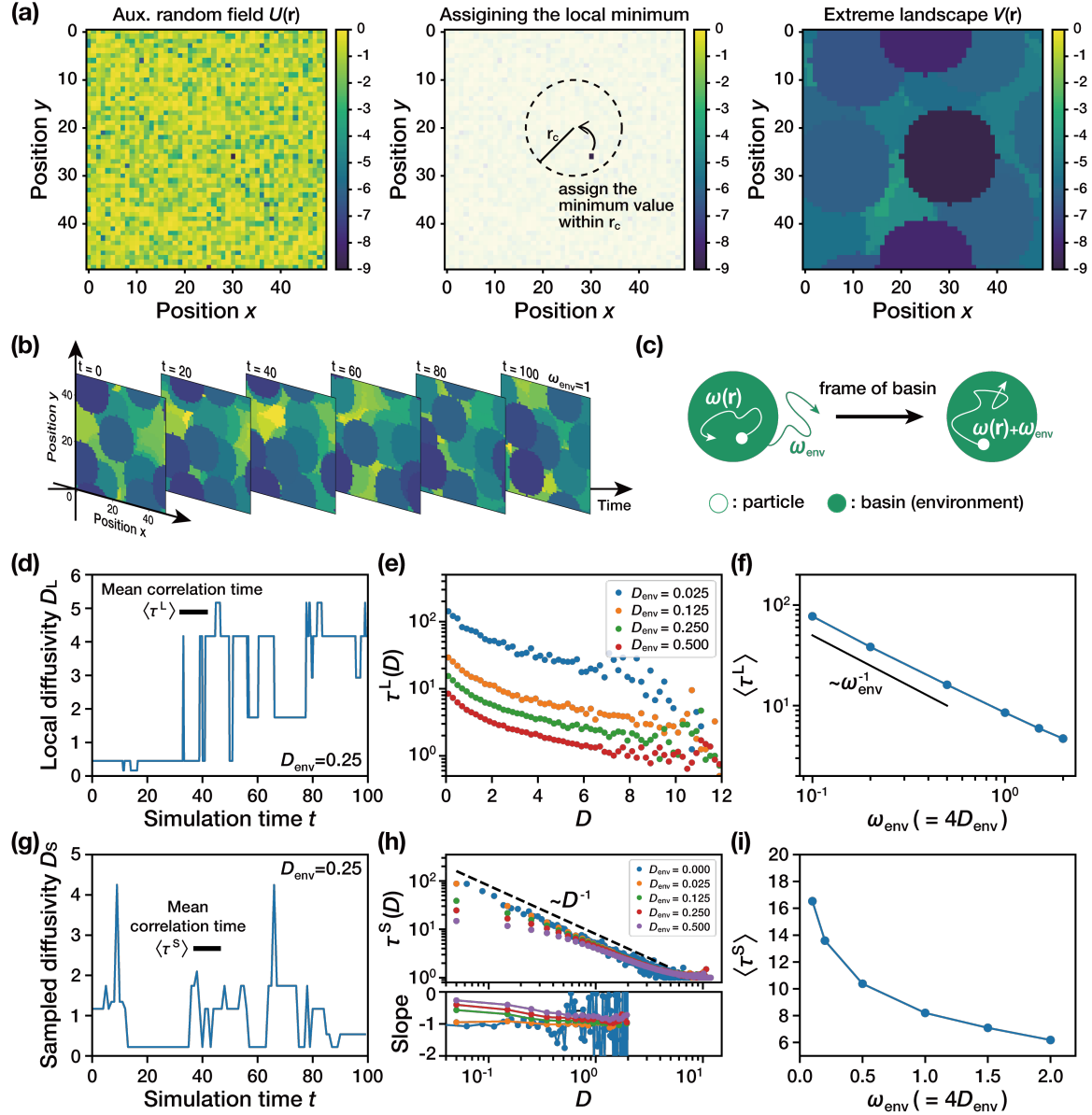


FIG. 1: **An annealed extreme landscape and its dynamic properties.** (a) Generation of an extreme landscape. In the left panel, an auxiliary random field is generated (with $L = 50$ in this figure) by assigning random energies to the lattice points, sampled from the exponential distribution (3). In the middle panel, for a given auxiliary field, the local energy minimum within a critical radius r_c is assigned to every lattice point. Finally, in the right panel, the resulting extreme landscape is constructed. (b) Time evolution of the annealed extreme landscape shown in (a). Here, $\omega_{\text{env}} = 1$. (c) Schematic illustrating a tracer particle diffusing in a basin of an annealed extreme landscape. The particle moves to an adjacent lattice point with the rate $\omega(\mathbf{r})$, while the environment changes with the rate ω_{env} . In the reference frame of the basin (right), a particle diffuses with the combined rate $\omega(\mathbf{r}) + \omega_{\text{env}}$ while the environment remains immobile. (d) An example of the time evolution of the local diffusivity at a fixed position \mathbf{r} with $D_{\text{env}} = 0.25$. The bold black line represents the duration of the mean residence time $\langle \tau^L \rangle = 8.52$. (e) PDF of residence times τ^L of the local diffusivity D for various values of D_{env} . (f) Mean residence times of the local diffusivities, $\langle \tau^L \rangle$, as a function of ω_{env} . The solid line depicts the scaling with the power-law $1/\omega_{\text{env}}$. (g) A simulated sampled diffusivity D_S for $D_{\text{env}} = 0.25$. The bold black line represents the mean correlation time $\langle \tau^S \rangle = 8.20$. (h) The distribution of residence times τ^S of the sampled diffusivities as a function of D for several values of D_{env} . The dashed line denotes the power-law scaling $1/D$. The bottom panel shows the fitted power-law slope for $\tau^S(D)$. (i) Mean residence times $\langle \tau^S \rangle$ of the sampled diffusivities, as a function of ω_{env} .

As a result of the above workflow, we obtain the annealed extreme landscape with the environmental diffusivity

$$D_{\text{env}} \equiv \frac{\omega_{\text{env}} a^2}{4t_0} = \frac{\omega_{\text{env}}}{4}. \quad (6)$$

Figure 1(b) depicts an exemplary annealed extreme landscape that evolves over time (here, $\omega_{\text{env}} = 1$ and $D_{\text{env}} = 0.25$).

B. Local diffusivity field

To describe the local trapping/escape dynamics on a given annealed extreme landscape $V(\mathbf{r}, t)$, we trace the diffusing dynamics of a tracer particle. The Kramers escape rate from the local trapping site \mathbf{r} at time t is given by

$$\omega(\mathbf{r}, t) = \omega_0 \exp[V(\mathbf{r}, t)], \quad (7)$$

where $\omega_0 = 4\pi r_c^2/(a^2 t_0)$ and, for simplicity, the ambient temperature $k_B T$ is set to unity. Our choice of ω_0 sets the escape rate at a local trap of depth V_0 to 4 per unit time ($t_0 = 1$), and the corresponding local diffusivity of the tracer becomes unity [a^2/t_0]. We find that the Kramers escape rates from the trapping sites follow the exponential law (see the derivation in App. B)

$$f_\omega[\omega(\mathbf{r}, t) = \omega] = \frac{t_0}{4} \exp\left(-\frac{\omega t_0}{4}\right). \quad (8)$$

After the escape, the particle hops onto one of its four nearest neighbor sites with equal probability of $1/4$.

In Fig. 1(c), we schematically illustrate the diffusion of a tracer particle (white dot) within an annealed extreme landscape. The particle hops onto the lattice with a jump rate of $\omega(\mathbf{r}, t)$ while the extreme landscape changes over time with the annealing rate ω_{env} (or the annealing diffusivity D_{env}) [Eq. (6)]. As these two contributions are independent of each other, the tracer's positional net change relative to an extreme basin occurs at a rate of $\omega(\mathbf{r}, t) + \omega_{\text{env}}$. Alternatively, the sojourn time of a particle at site \mathbf{r} within an extreme basin is given by

$$\tau(\mathbf{r}, t) = \frac{1}{\omega(\mathbf{r}, t) + \omega_{\text{env}}}. \quad (9)$$

Using a change of variables (App. B), the PDF of sojourn times $\tau \in (0, \omega_{\text{env}}^{-1})$ is obtained as

$$f_\tau[\tau(\mathbf{r}, t) = \tau] = \frac{\tau_0 \exp(\omega_{\text{env}} \tau_0)}{\tau^2} \exp\left(-\frac{\tau_0}{\tau}\right), \quad (10)$$

where $\tau_0 = t_0/4$. Accordingly, the stationary positional PDF of tracer particles is given by

$$\pi(\mathbf{r}, t) = \frac{\tau(\mathbf{r}, t)}{\sum_{\mathbf{r}'} \tau(\mathbf{r}', t)} \quad (11)$$

in terms of the sojourn time PDF (9).

We then define the local diffusivity of the tracer particles in the annealed extreme landscape as

$$D_L(\mathbf{r}, t) = \frac{\omega(\mathbf{r}, t) a^2}{4} = \pi r_c^2 \exp[V(\mathbf{r}, t)]. \quad (12)$$

This relation indicates that the local diffusivity field is solely determined by the spatiotemporal heterogeneity of the extreme landscape. The PDF of local diffusivities on the annealed extreme landscape reads

$$\psi_L(D_L = D) = \frac{1}{D_0} \exp\left(-\frac{D}{D_0}\right), \quad (13)$$

as obtained via Eq. (5), where $D_0 = \omega_0 a^2 \exp(V_0)/4 = 1$.

In Fig. 1(d), we plot the time evolution of the local diffusivity $D_L(\mathbf{r}, t)$ at a fixed point \mathbf{r} from stochastic simulations. It is observed that the local diffusivity exhibits significant fluctuations in time due to the annealed dynamics of the extreme landscape. Using the time traces of the simulated local diffusivities, we compute the average residence time for a given value of D_L . Figure 1(e) presents the relation of the residence time vs. D_L . We find that a larger value D_L (associated with a shallower V) has a shorter residence time τ^L . This inverse behavior stems from the fact that the shallow potential traps, which are overshadowed by the deeper ones, have smaller spatial correlation lengths, as illustrated in Fig. 1(a) or (b), and the particle diffuses faster over these shallow potential regions. In Fig. 1(f), we plot the mean residence time $\langle \tau^L \rangle$ against the annealing rate. The mean residence time $\langle \tau^L \rangle$ is found to be, approximately, inversely proportional to ω_{env} .

C. Sampled diffusivity

We now define the sampled diffusivity $D_S(t)$ as the time sequence of the local diffusivities that a diffusing tracer visits over time; see Fig. 1(g) for an example. As the tracer particle diffuses on a random landscape, $D_S(t)$ in general is temporally fluctuating and reflecting the correlated nature of the local diffusivity field. In this sense, the stochastic behavior of the sample diffusivity is reminiscent of the diffusivity dynamics in the fluctuating diffusivity model [28, 30, 43] or the annealed transit time model (ATTM) [64].

In Fig. 1(h), we numerically estimate the relationship between the residence time $\tau^S(D)$ of the sampled diffusivity against its value D . For various annealing rates, a general tendency is that the larger the sampled diffusivity D the shorter its residence time $\tau^S(D)$. In particular, in the limit of a fully quenched landscape ($D_{\text{env}} \rightarrow 0$), the residence time PDF has the power-law scaling $\tau^S(D) \sim D^{-\gamma}$ with $\gamma \approx 1$ within our observation time window. A similar relation between the diffusivity and its residence time is defined in the annealed transit time model (ATTM) in which the residence time for a

given diffusivity D follows a power-law relation with the expectation $\mathbb{E}[\tau|D] \sim \tau^{-\gamma}$ [64]. As the annealing of the system gets more pronounced ($\omega_{\text{env}} \gg 1$), the overall behavior of τ^S deviates from the simple power-law scaling, because the annealing induces the release of a particle from a deep local trap.

The relationship between the PDFs $\psi_S(D_S)$ of the sampled diffusivity and $\psi_L(D_L)$ of the local diffusivity can be derived as follows. Given that a particle sits on a site with $D_L = \frac{\omega a^2}{4}$, the particle's sojourn time at this site is $\tau = 1/(\omega + \omega_{\text{env}})$ [Eq. (9)]. Therefore, the PDF of the sampled diffusivity $D_S = D$ is obtained as

$$\begin{aligned} \psi_S(D_S = D) &\propto \frac{1}{\omega + \omega_{\text{env}}} \times \text{total area associated with } D \\ &\propto \frac{\psi_L(D_L = D)}{D + D_{\text{env}}}. \end{aligned} \quad (14)$$

We note that in the quenched limit ($D_{\text{env}} \rightarrow 0$), the above relationship recovers the result reported in Ref. [43] for the quenched extreme landscape,

$$\psi_S(D_S = D) \propto \frac{\psi_L(D)}{D}. \quad (15)$$

In Fig. 2(a), we show the distribution of the sampled diffusivity acquired from stochastic simulations (symbols) for several values of $\omega_{\text{env}} (= 4D_{\text{env}}/a^2)$. The simulated data is in excellent agreement with the expected sampled diffusivity PDF (14), depicted as the dashed lines.

A notable effect of the environmental change (quantified by D_{env}) is the reduced probability for sampling small-valued diffusivities. In the quenched landscape, a particle spends a long time escaping from a region of slow diffusivity. In contrast, in an annealed environment, a trapped particle can escape more quickly from such regions because the environment itself changes. Consequently, the mean sampled diffusivity of a particle increases in an annealed landscape. The mean sampled diffusivity $\langle D_S \rangle$ of a particle is obtained as

$$\langle D_S \rangle = D_0 \frac{\exp(-D_{\text{env}}/D_0)}{\Gamma(0, D_{\text{env}}/D_0)} - D_{\text{env}}, \quad (16)$$

where $\Gamma(s, x) = \int_x^\infty t^{s-1} e^{-t} dt$ is the upper incomplete Gamma function [65]. In Fig. 2(b), we plot the mean sampled diffusivity $\langle D_S \rangle / D_0$ against D_{env} / D_0 . Notably, the mean diffusivity $\langle D_S \rangle$ monotonically increases with increasing D_{env} , converging to D_0 in the large- D_{env} limit. This trend is indeed observed in our simulation video [66], where the tracers attain a faster diffusivity as D_{env} increases. We also note that the mean sampled diffusivity converges to zero in the quenched limit $D_{\text{env}} \rightarrow 0$ [Eq. (16)]. This happens because the diffusing tracers end up highly immobilized in regions where $V(\mathbf{r}) \rightarrow -\infty$. However, such an infinite trap cannot be realized in a finite system ($L < \infty$), in which the particles remain mobile even when D_{env} is negligible (but finite). In previous studies on the quenched extreme landscape [44, 45],

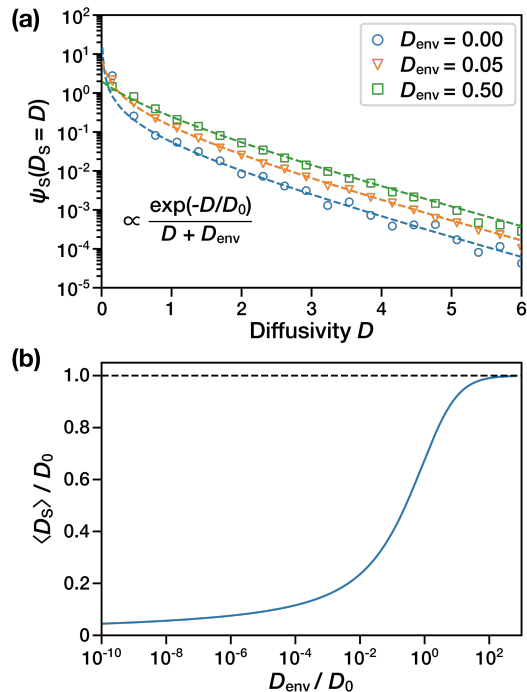


FIG. 2: **Profiles and the mean values of the sampled diffusivities.** (a) Normalized PDF $\psi_S(D)$ of the sampled diffusivities for various values of D_{env} . The simulation results (symbols) are in excellent agreement with the theoretical PDF (14) depicted as the dashed lines. (b) Theoretical result [Eq. (16)] for the mean sampled diffusivities $\langle D_S \rangle / D_0$ as function of D_{env} . The dashed line shows the limiting value for $D_{\text{env}} \rightarrow \infty$.

it was demonstrated that the longest sojourn time of a diffusing tracer scales as $\tau \sim L^2$ and the mean sampled diffusivity is inversely proportional to the logarithm of the system size, $\langle D_S \rangle \propto 1/\log L^2$.

III. FICKIAN YET NON-GAUSSIAN DIFFUSION

A. Mean squared displacements

To characterize the diffusion dynamics of tracers in extreme energy landscapes, we first estimate the MSDs from the simulated trajectories. Figs. 8(a), (b) show the MSDs of tracers in quenched and annealed landscapes, respectively. Each case was simulated with stationary initial positions of tracers according to Eq. (11) for $N_{\text{par}} = 1000$ tracers. In the plot, the gray solid lines represent 500 time-averaged (TA) MSD curves from individual trajectories according to the definition [13, 67]

$$\overline{\delta^2(\Delta)} = \frac{1}{T - \Delta} \int_0^{T-\Delta} dt [x(t + \Delta) - x(t)]^2, \quad (17)$$

and the thick line (black) represents their ensemble-average (EA), $\langle \delta^2(\Delta) \rangle$, the EATAMSD. Here, Δ represents the lag time, the magnitude of the sliding window, and T stands for the total observation time or length of the time series $x(t)$. For comparison, in Fig. 8, we also calculate the conventional (EA) MSD¹

$$\langle \Delta x(t)^2 \rangle = \frac{1}{N_{\text{par}}} \sum_{i=1}^{N_{\text{par}}} [x_i(t) - x_i(0)]^2 \quad (18)$$

shown by the circles (\circ).

In both the quenched ($D_{\text{env}} = 0$) and annealed ($D_{\text{env}} = 0.5$) cases, the EATAMSD and MSDs coincide with each other and increase linearly with time throughout the observation time window. These results suggest that the tracers in heterogeneous random environments exhibit Fickian diffusion regardless of the detail of the spatiotemporal heterogeneity. We note that the individual TAMSDs also follow the linear time evolution and that their amplitude scatter is very narrow (apart from long lag times $\Delta \rightarrow T$ when the statistic naturally deteriorates). This latter behavior is obtained when the total observation time T is sufficiently longer than the so-called homogenization time τ_c , that will be introduced below in Sec. IV. In the opposite regime $T \ll \tau_c$, the tracers explore locally distinct random environments, leading to noticeable trajectory-to-trajectory amplitude scatter in the TAMSD. For instance, see the MSDs for $T = 2 \times 10^3$ ($< \tau_c \approx 10^4$) in Fig. 8a (which will be discussed in detail below).

The observed Fickian diffusion can be explained as follows: At short times $t' \ll \langle \tau^S \rangle$, the diffusivity D_S sampled by a particle remains approximately a constant, such that the diffusion is Fickian and $\mathbb{E}[[x(t') - x(0)]^2] \approx 2D_S t'$. Therefore, the MSD from a collection of tracers for the time range t' can be simply written as

$$\begin{aligned} \langle [x(t') - x(0)]^2 \rangle &\approx 2\langle D_S \rangle t' \\ &= 2a^2 \left\langle \frac{\omega t'}{4} \right\rangle = \frac{a^2}{2} \langle n(t') \rangle. \end{aligned} \quad (19)$$

Here, $n(t')$ denotes the number of steps of the random walk performed by the particle during the time interval $[0, t']$, and the average $\langle \dots \rangle$ is taken over an ensemble of the stationary initial condition. Given that the ensemble is in the stationary state, the MSD over the time interval $[t', 2t']$ is also given by $\langle [x(2t') - x(t')]^2 \rangle \approx a^2 \langle n(t') \rangle / 2$, meaning that the same number of random walk steps approximately occur during $[t', 2t']$. Therefore, for an arbitrary $t > 0$, the number of random walk steps during the time interval $[0, t]$ is $\langle n(t) \rangle = \langle n(t') \rangle \times (t/t')$. Plugging this relation into Eq. (19), the MSD at time t is obtained as

$$\langle \Delta x(t)^2 \rangle \approx 2\langle D_S \rangle t. \quad (20)$$

¹ In the following referred to simply as the MSD.

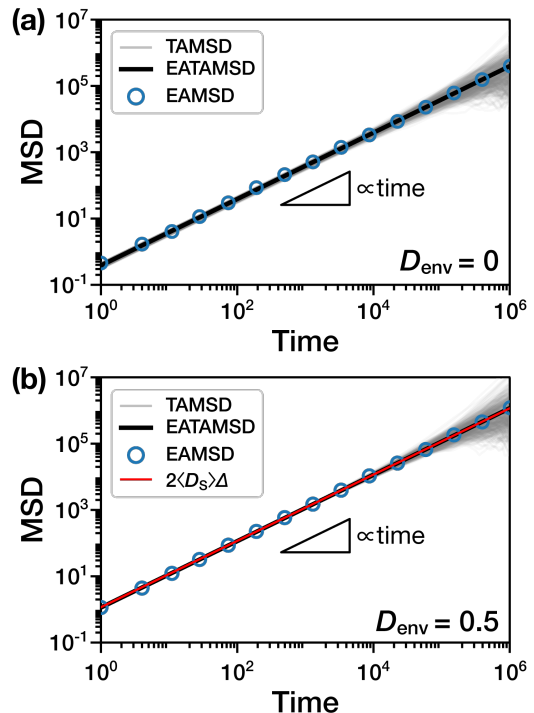


FIG. 3: **Mean squared displacement estimates from stochastic simulations.** (a) MSDs from simulated trajectories ($N_{\text{par}} = 1000$, $T = 2 \times 10^6$) for the quenched extreme landscape ($D_{\text{env}} = 0$). Individual TAMSDs (grey lines), MSD (blue circles), and EATAMSD (black line) overlap nicely and exhibit Fickian (normal) diffusion. (b) MSDs ($N_{\text{par}} = 1000$, $T = 2 \times 10^6$) for an annealed extreme landscape ($D_{\text{env}} = 0.5$). The individual TAMSDs (grey lines), MSD (blue circles), and EATAMSD (black line) again exhibit Fickian behavior, as predicted by the theoretical result (20). For the simulations in the panels of (a) and (b), the initial distribution of the tracer particles was chosen according to the stationary distribution given by Eq. (11).

This result suggests that for stationary initial conditions the MSD (along with the EATAMSD) satisfy the Fickian diffusion law with the diffusivity given by the ensemble-averaged sampled diffusivity $\langle D_S \rangle$. This is indeed confirmed in Fig. 8(b) where our theory Eq. (20) perfectly explains the simulated MSD and EATAMSD in the annealed random system ($D_{\text{env}} \neq 0$). In the case of a non-stationary initial condition, the MSDs exhibit short-time Fickian diffusion with a diffusivity that depends on the initial distribution of the sampled diffusivity. Thus, in general, the non-stationary Fickian diffusion observed is different from Eq. (20). Moreover, a non-Fickian diffusion emerges during the cross-over time before converging to the stationary behavior (20) after homogenization. Further discussion on this point is presented in App. C, see Fig. A1.

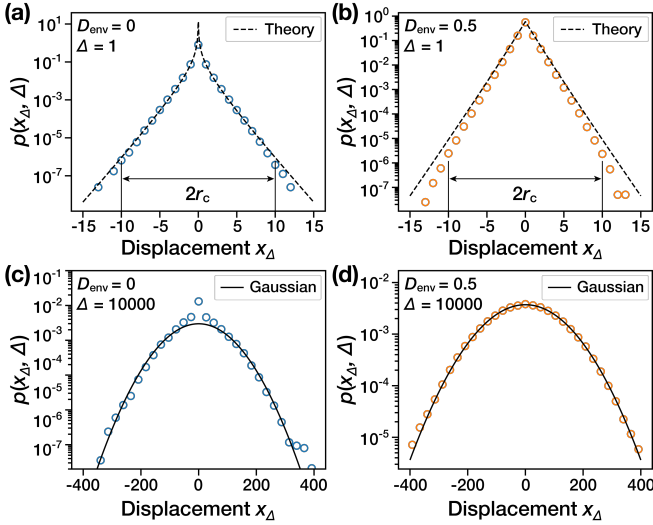


FIG. 4: **Van-Hove self-correlation functions from the simulated trajectories.** (a) and (b): Van-Hove self-correlation function extracted from stochastic simulations (symbols, $N_{\text{par}} = 1000$) at lag time $\Delta = 1$ for (a) a quenched extreme landscape ($D_{\text{env}} = 0$) and (b) an annealed extreme landscape ($D_{\text{env}} = 0.5$). The black dashed lines denote the analytic result (23). (c) and (d): Van-Hove self-correlation function (symbols, $N_{\text{par}} = 1000$) at lag time $\Delta = 10^4$ for (c) a quenched extreme landscape ($D_{\text{env}} = 0$) and (d) an annealed extreme landscape ($D_{\text{env}} = 0.5$). In both panels (c) and (d), the black solid lines show the best Gaussian fit to the data.

B. Van-Hove self-correlation function

We next examine the distribution of tracer displacements in both the quenched and annealed landscapes studied above. For each case, the Van-Hove self-correlation function $p(x, \Delta)$ is calculated for the ensemble of tracers at a short ($\Delta = 1$) and long ($\Delta = 10^4$) lag times and shown in Fig. 3. We note that while the MSDs are Fickian, the heterogeneous diffusion of the tracers is highly non-Gaussian. In the quenched environment, the Van-Hove self-correlation function has a sharp cusp at the center and decays exponentially. The cusp originates from immobile tracers trapped in deep potential wells. The escape of these tracers from the traps occurs at long time scales. Thus, the cusp remains persistent even when the lag time becomes substantial ($\Delta = 10^4$).

Notably, in the annealed random environment, the tracer diffusion exhibits a non-Gaussian behavior analogous to the fluctuating diffusivity model [28]. On short time scales, the tracer displacement follows the Laplace distribution (shown here for $\Delta = 1$). The Laplace Van-Hove self-correlation function crosses over to a Gaussian at long time scales when $t \gtrsim \tau_c$. In Fig. 3(d), the simulation data is perfectly fitted by a Gaussian. Summarizing the results of the MSD and displacement PDF, we find that in an annealed extreme landscape the tracer exhibits Fickian yet non-Gaussian diffusion reported in heteroge-

neous diffusion phenomena in various soft matter and biological systems.

To explain the non-Gaussian diffusion and its crossover to a Gaussian behavior, we start by considering the diffusion of a single tracer. For time intervals shorter than $\langle \tau^S \rangle$, the sampled diffusivity D_S of the tracer remains almost constant. On this time scale, the single tracer diffusion is normal with the Gaussian propagator

$$G(x, \Delta | D_S) = \frac{1}{\sqrt{4\pi D_S \Delta}} \exp\left(-\frac{x^2}{4D_S \Delta}\right), \Delta \lesssim \langle \tau^S \rangle. \quad (21)$$

When $\Delta \gg \langle \tau^S \rangle$, the above Gaussian limit no longer holds as the tracer explores the spatiotemporally varying local diffusivity field. Conversely, on time scales at which the Gaussian approximation (21) holds, the van-Hove self-correlation function $p(x_\Delta, \Delta)$ can be evaluated via a superstatistical approach [28, 30, 39]. Using the PDF ψ_S from Eq. (14) of the sampled diffusivity, it can be simply written as

$$p(x_\Delta, \Delta) = \int_0^\infty dD_S G(x_\Delta, \Delta | D_S) \psi_S(D_S), \quad (22)$$

where $x_\Delta \lesssim r_c$ and $\Delta \lesssim \langle \tau^S \rangle$. Performing this superstatistical integral above, we obtain the analytic expression for the Van-Hove self-correlation function in the form

$$p(x_\Delta, \Delta) \propto \sqrt{\frac{\pi}{4D_{\text{env}} \Delta}} \operatorname{erfc}\left(\frac{|x_\Delta|}{2\sqrt{D_{\text{env}} \Delta}} + \sqrt{\frac{D_{\text{env}}}{D_0}}\right) \times \exp\left(\frac{x_\Delta^2}{4D_{\text{env}} \Delta} + \frac{D_{\text{env}}}{D_0}\right), \quad (23)$$

where $\operatorname{erfc}(y) = (2/\sqrt{\pi}) \int_y^\infty \exp(-t^2) dt$ is the complementary error function. The derivation of Eq. (23) is detailed in App. D. In Figs. 3(a) and (b), the above theoretical approximation is shown as the dashed line along with the simulations data. At short time $\Delta = 1$, for which the superstatistics is valid, the theoretical curve successfully explains the data, corresponding to $|x_\Delta| \lesssim r_c$. This expression deviates from the data, as expected, when $|x_\Delta| \gtrsim r_c$ in the tail part as the particles traverse multiple extreme basins beyond the correlation length of the order of r_c .

We obtain further insight into the intricate behavior of the Van-Hove self-correlation function (23) by simplifying it under the condition $\Delta \ll |x_\Delta|^2 D_{\text{env}}^{-1}$, which yields

$$p(x_\Delta, \Delta) \approx \mathcal{N} \frac{\exp\left(-\frac{|x_\Delta|}{\sqrt{D_0 \Delta}}\right)}{|x_\Delta| + 2D_{\text{env}} \sqrt{\Delta/D_0}}, \quad (24)$$

where \mathcal{N} is the normalization factor. With this result, the essential form of the van-Hove function is attained as follows: (1) in the quenched limit, the environmental fluctuations are negligible ($D_{\text{env}} \approx 0$) and $|x| \gg 2D_{\text{env}} \sqrt{\Delta/D_0}$. Hence, the Van-Hove self-correlation function simplifies to

$$p(x_\Delta, \Delta) \propto \frac{1}{|x_\Delta|} \exp\left(-\frac{|x_\Delta|}{\sqrt{D_0 \Delta}}\right), \quad (25)$$

reproducing the analytic form reported in Ref. [45]. The prefactor $|x_\Delta|^{-1}$ accounts for the cusp at the center observed in the simulations results shown in Fig. 3(a). (2) In the strong annealing limit (i.e., $|x| \ll 2D_{\text{env}}\sqrt{\Delta/D_0}$), when the environmental change is significantly larger than the particle diffusion, the Van-Hove self-correlation function behaves as a Laplace distribution,

$$p(x_\Delta, \Delta) \propto \exp\left(-\frac{|x_\Delta|}{\sqrt{D_0\Delta}}\right), \quad (26)$$

as seen in Fig. 3(b).

The theoretical Van-Hove self-correlation functions (23) to (26) are valid when the superstatistical average can be applied, on time scales $< \tau^S$. The exponential-like van-Hove function changes into the Gaussian profile at times much longer than the homogenization time τ_c , see the plots of $p(x_\Delta, \Delta)$ at $\Delta = 10,000$ in Figs. 3(c) and (d). Here, the tracer samples a large number of instantaneous diffusivities over a large distance, crossing a correlation time analogously to the crossover to Gaussian behavior in the fluctuating diffusivity model. The tail of $p(x_\Delta, \Delta)$ then gradually approaches a Gaussian PDF, in line with the central limit theorem. In particular, for the annealed case (Fig. 3(d)), the environmental fluctuations assist the localized tracer in escaping from deep traps, which results in a perfect Gaussian distribution, while in the quenched case a cusp persists at the origin (Fig. 3(c)).

C. Non-Gaussianity Parameter

We continue to examine the deviations from Gaussianity of the spatiotemporally heterogeneous diffusion process on the disordered energy landscape in terms of the non-Gaussianity parameter (i.e., the excessive kurtosis), for a centered PDF,

$$\text{NGP} = \frac{1}{3}\text{Kurt}[x] - 1 = \frac{1}{3}\frac{\langle x^4 \rangle}{\langle x^2 \rangle^2} - 1 \quad (27)$$

where Kurt is the kurtosis [13], and x is one of the Cartesian components in \mathbf{r} . Due to the finite-observation time effects shown in the tail part of the Van-Hove self-correlation functions, we here employ the modified NGP (mNGP)

$$\widehat{\text{NGP}} = \text{NGP} - \text{NGP}_0. \quad (28)$$

Here NGP_0 represents the NGP for a truncated normal distribution defined on the interval $[-\sqrt{2\log(N_{\text{tr}}T/\Delta)}, \sqrt{2\log(N_{\text{tr}}T/\Delta)}]$ in which N_{tr} denotes the number of sample trajectories used in the analysis. The validity of $\widehat{\text{NGP}}$ for the analysis of non-Gaussianity in our system is demonstrated in detail in App. E.

Figure 5(a) shows the variation of $\widehat{\text{NGP}}$ with lag time Δ from simulated trajectories for varying D_{env} . It

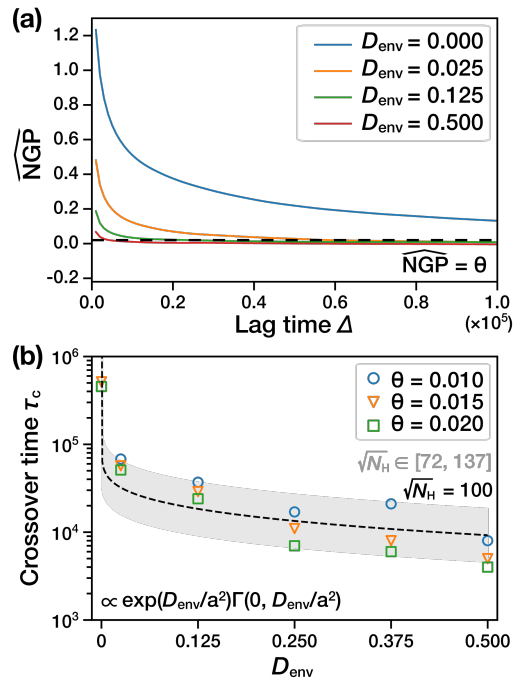


FIG. 5: **Estimation of the non-Gaussianity and the crossover time.** (a) $\widehat{\text{NGP}}$ [Eq. (28)] as function of the lag time Δ for several values of D_{env} . Each curve was obtained from 10^3 simulated trajectories of length $T = 2 \times 10^6$. The horizontal dashed line depicts the threshold value $\theta = 0.025$, see Eq. (29). (b) Crossover time τ_c [Eq. (29)] against D_{env} for three threshold values θ . The gray shade indicates the region of theoretical homogenization times [Eq. (35)] with $\sqrt{N_{\text{H}}} \in [72, 137]$. The black dashed line depicts the theoretical formula (35) for the homogenization time, for $\sqrt{N_{\text{H}}} = 100$.

demonstrates that for all cases the tracers perform non-Gaussian diffusion at short times with a positive value of $\widehat{\text{NGP}}$. The mNGP gradually decays towards zero as Δ increases. The tracer motion tends to recover Gaussianity faster with increasing D_{env} , as here the environmental fluctuations help the immobile tracer to escape from the trapped site.

We define the crossover time τ_c at which the short-time non-Gaussianity crosses over to a Gaussian diffusion,

$$\tau_c = \min \left\{ \Delta \mid \widehat{\text{NGP}} = \theta \right\}, \quad (29)$$

as estimated by the threshold value θ (corresponding to the dashed line in Fig. 5(a) for $\theta = 0.025$). That is, the time scale τ_c refers to the moment when the NGP reaches the threshold value θ for the first time. In Fig. 5(b), we plot τ_c against D_{env} for three values of θ . We observe that regardless of the threshold values the estimated value of τ_c displays consistent variations with D_{env} . Namely, the crossover times gradually decrease with D_{env} in the range from 10^4 to 10^5 . It turns out that the estimated values are in good agreement with the homogenization time that the Gaussian distribution is recovered in the Van-Hove self-correlation function $p(x_\Delta, \Delta)$. For instance, the an-

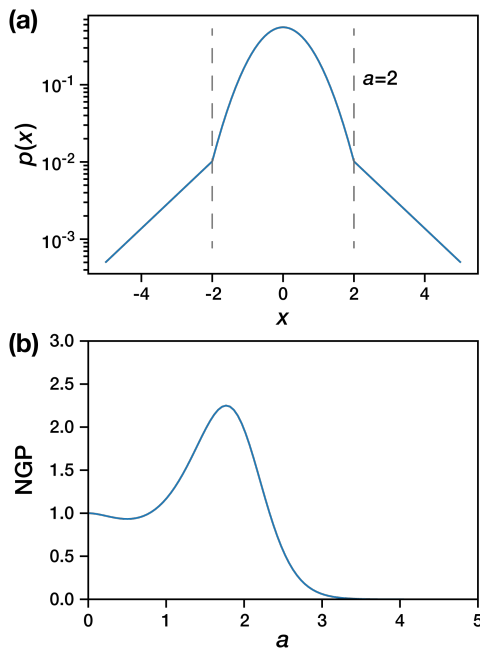


FIG. 6: (a) The composite PDF (30) with a Gaussian core and far Laplace tails for $a = 2$. (b) Corresponding NGP (i.e., the excessive kurtosis) as a function of the width a of the central Gaussian core. Already for $a \approx 3$, NGP is approximately zero, as the weight of the Laplace tails becomes negligible.

nealed system with $D_{\text{env}} = 0.5$ is found to have $\tau_c \approx 10^4$, which is in good agreement with the value in Fig. 3(d) in which $p(x_\Delta, \Delta)$ has a Gaussian profile at $\Delta = 10^4$. In the following Section, we present the concept of homogenization and an analytic theory accounting for the timescale τ_c in terms of the relevant system parameters of the annealed extreme landscape.

We stop to note that a zero value of the non-Gaussianity parameter does not necessarily mean that the far tails of a PDF are indeed Gaussian. Namely, if the PDF has a dominant central Gaussian component, the contributions to the non-Gaussianity parameter of far non-Gaussian tails may simply become negligible, despite being present in the PDF. This can be shown, e.g., by calculating NGP for the composite PDF [68]

$$p(x) = \mathcal{N} \left[e^{-a+a^2-x^2} \theta(a-|x|) + e^{-|x|} \theta(|x|-a) \right], \quad (30)$$

in which \mathcal{N} is the normalization constant and $\theta(x)$ is the Heaviside step function. At a , that is, exponential tails are connected to a central Gaussian. The composite PDF (30) along with the NGP is shown in Fig. 6. We see that for $a = 0$, i.e., a single Laplace PDF, the limiting value $\text{NPG} = 1$ is reached, transiently increases for growing a , until it finally reaches the value $\text{NPG} = 0$. This value is approximately realized at $a = 3$, despite the far Laplace tails.

IV. HOMOGENIZATION OF THE ENVIRONMENT AND ERGODICITY

As investigated in the previous Section, the short time non-Gaussian diffusion in the heterogeneous extreme landscape eventually approaches an effective Gaussian shape over time. This crossover from a non-Gaussian to a Gaussian PDF in the long-time regime is termed *homogenization*. We now focus on this homogenization process, before addressing the ergodicity breaking parameter of the dynamics.

A. Homogenization

One can anticipate that in an annealed random environment the tracer particle initially is determined by the spatiotemporally heterogeneous diffusion. Once, however, the tracer has explored a sufficient fraction of distinct sites of a given diffusivity field, it has sampled a substantial fraction of the given random environment and thus reaches an effectively homogeneous Gaussian PDF with a mean diffusivity. This is what we refer to as the homogeneous process. If the diffusivity field is self-similar such that a part of the entire field mirrors the whole random diffusivity landscape, we may expect that sampling this partial diffusivity field suffices for a tracer particle to achieve homogenization.

As an example to demonstrate this idea, we present in Fig. 7(a) a simulated diffusivity field $\{D_L\}$ of size N_{tot} (blue box, $N_{\text{tot}} = 512^2$) with several subsets of size N_H depicted as the red boxes. The local diffusivity field in the subset is defined as a square box with a side length of $\sqrt{N_H}$. Distinct subsets are created using a sliding window with the periodic boundary condition (the dashed boxes in Fig. 7(a)), resulting in a total of L^2 sliding windows. For each subset diffusivity field, we measure the mean local diffusivity $\langle D_L \rangle$ within the window. If a subset of size N_H is a self-similar representation of the entire environment, the mean local diffusivities from distinct subsets will not differ much from each other, i.e., exhibiting a small deviation from the diffusivity of the entire field. However, if the system is not self-similar or the subset size is not sufficiently large, the system will display substantial deviations in their mean local diffusivities.

We define the relative standard deviation (RSD) of the mean local diffusivities

$$\text{RSD}(\langle D_L \rangle) = \frac{\sqrt{\mathbb{E}[\langle D_L \rangle^2] - \mathbb{E}[\langle D_L \rangle]^2}}{\mathbb{E}[\langle D_L \rangle]}, \quad (31)$$

where $\mathbb{E}[\dots]$ denotes ensemble-averaging over the distinct sliding windows. Figure 7(b) shows a numerical estimate for RSD as a function of $\sqrt{N_H}$ (solid line). The RSD monotonically decays with the size of the subset diffusivity field, supporting the idea of the discussed self-similarity property. The result shows that the decrease of RSD tends to follow an exponential decay with $\sqrt{N_H}$.

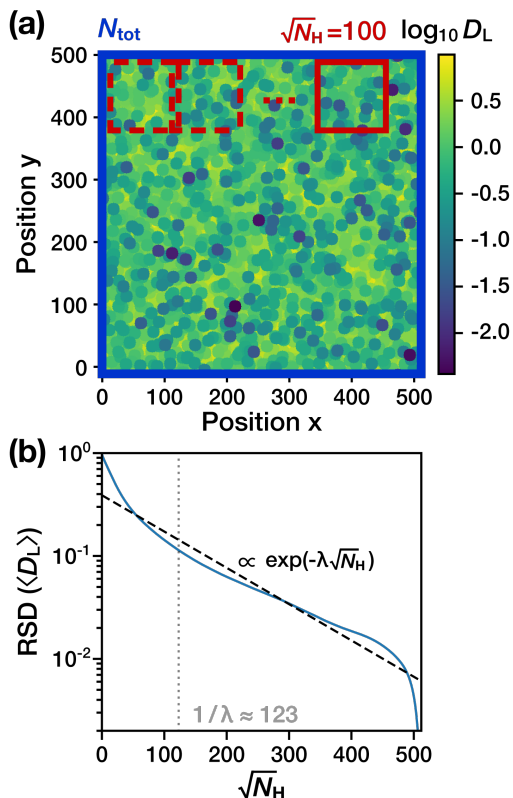


FIG. 7: **Analysis of the self-similarity of the extreme landscape.** (a) Simulated local diffusivity field (blue box) with samples of a subset field of size N_H (red box). Using the sliding window (depicted as the dashed boxes in the plot) with periodic boundary condition, a total of $L^2 = 512^2$ subsets are defined. (b) Relative standard deviation (RSD) of the mean local diffusivities, Eq. (31), as a function of the window size N_H (solid line). The dashed line represents an exponential decay $\propto \exp(-\lambda\sqrt{N_H})$ with a best fit value $\lambda = 0.0081$. The dotted line denotes the characteristic constant $1/\lambda \approx 123$ for $\sqrt{N_H}$. See text for details.

Fitting with an exponential function $\propto \exp(-\lambda\sqrt{N_H})$ (dashed line) reveals that $1/\lambda \approx 123$ is the characteristic size of a subset field to ensure sufficient self-similarity. Namely, if the local subset field explored by a tracer is larger than the characteristic size, the RSD exponentially decreases to zero, indicating that the tracer has almost the same mean diffusivity regardless of the position of the sampling subset field.

We now conceive a theoretical description for the homogenization time based on the idea of the self-similar local field. Let $N_{\text{tot}} = L^2$ be the total number of lattice sites of our diffusivity field and N_H be the number of distinct lattice sites visited by the tracer as required for achieving homogenization. As argued above, the local sites included in the field N_H are sufficient to capture the essential features of the spatiotemporally heterogeneous landscape of the entire field. We also define M as the number of steps required for a tracer to visit N distinct sites during its random walk. On a 2D lattice, the av-

erage number of distinct sites N visited by M random steps is known to be [69]

$$N \approx \frac{\pi M}{\log(8M)}. \quad (32)$$

Based on this expression, we derive the average number of visits γ to every distinct site after M random steps as a function of N ,

$$\gamma(N) \equiv \frac{M}{N} = -\frac{1}{\pi} W\left(-\frac{\pi}{8N}\right), \quad (33)$$

where $W(x)$ denotes the Lambert W-function [70]. From this relation, the time τ_c required to sample N_H distinct sites can be obtained on the mean-field level as

$$\begin{aligned} \tau_c &\approx \gamma(N_H) \frac{N_H}{N_{\text{tot}}} \sum_{\mathbf{r}}^{N_{\text{tot}}} \tau[\omega(\mathbf{r})] \\ &\approx \gamma(N_H) \frac{N_H}{N_{\text{tot}}} \int_0^\infty d\omega \frac{N_{\text{tot}}}{\omega + \omega_{\text{env}}} f_\omega. \end{aligned} \quad (34)$$

In the last expression the summation term is approximated by an integral, in which $f_\omega = \exp(-\omega/4)/4$ is the density of states. Performing the integral, we obtain the analytic expression for τ_c in terms of the annealing rate (D_{env}) and the size of a self-similar subset field in the form

$$\tau_c = \frac{\gamma(N_H)N_H}{4} \exp\left(\frac{D_{\text{env}}}{a^2}\right) \Gamma\left(0, \frac{D_{\text{env}}}{a^2}\right). \quad (35)$$

Here, $\Gamma(s, x)$ is the upper incomplete gamma function explained above in Eq. (16).

We validate our analytical result (35) with stochastic simulations. Fig. 5(b) shows the simulated crossover times at which the initial non-Gaussian diffusion is crossing over to Gaussian dynamics in terms of the mNGP, with the criterion (29), for various annealed extreme landscapes. These cross-over times are fitted with Eq. (35) in which N_H is a free parameter. We see that our analytic results reproduces nicely the measured crossover times with $\sqrt{N_H} \approx 100$ (dashed line). The gray shade region depicts the range of the subset size, $\sqrt{N_H} \in [72, 137]$, that is used for simulating the cross-over times τ_c against D_{env} for different thresholds θ .

B. Ergodicity breaking parameter

In addition to the temporal heterogeneity from a single trajectory, we now investigate another inherent form of heterogeneity, i.e., the heterogeneity from one trajectory to another [30]. In the preceding Section, we introduced the homogenization time τ_c accounting for the time scale at which the temporal heterogeneity is effectively averaged out. Beyond this timescale, the tracers exhibit a homogeneous Gaussian diffusion pattern. In

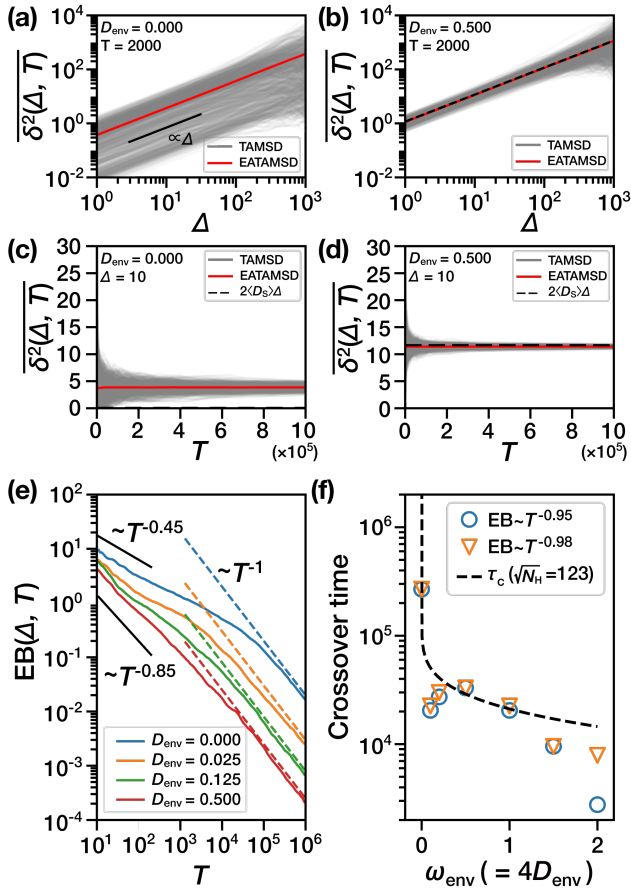


FIG. 8: **Particle-to-particle heterogeneity and ergodicity breaking parameter.** (a, b): Individual TAMSDs (gray) as a function of lag time Δ and corresponding ensemble-average (EATAMSD, red). (a) $D_{\text{env}} = 0$ (quenched). (b) $D_{\text{env}} = 0.5$ (annealed). (c, d) TAMSDs as a function of T at $\Delta = 10$. (c) $D_{\text{env}} = 0$ (quenched). (d) $D_{\text{env}} = 0.5$ (annealed). (e) EB parameter [Eq. (36)] as a function of T for various values of D_{env} . The solid black lines depict the two empirical power-laws $T^{-0.45}$ and $T^{-0.85}$, the dashed lines represent the power-law T^{-1} . (f) Crossover times beyond which the EB parameter begins to decay as $\simeq T^{-\theta_{\text{EB}}}$, with $\theta_{\text{EB}} = 0.95$ (blue) and 0.98 (orange). The dashed line indicates the theoretical homogenization time τ_c [Eq. (35)] with $\sqrt{N_H} = 100$.

the regime $t \lesssim \tau_c$, in contrast, individual particles display pronounced trajectory-to-trajectory heterogeneity, due to the distinct explored local energy landscape.

Figs. 8(a), (b) show TAMSDs versus the lag time for simulated individual trajectories when $D_{\text{env}} = 0$ and $= 0.5$. In both panels, EATAMSD is also shown (red lines). On the one hand, a substantial heterogeneity is visible between individual trajectories when the environment is quenched ($D_{\text{env}} = 0$) and the observation time $T (= 2000)$ is much shorter than the homogenization time τ_c . On the other hand, the annealing of the random landscape may significantly reduce the trajectory-to-trajectory heterogeneity even for short T , as seen in

Fig. 8(b). In Figs. 8(c), (d), we display the TAMSDs against T for a given Δ . As expected, the variation in the TAMSDs is larger in the quenched case as compared to the annealed case, and generally the TAMSD amplitude variations tend to be reduced as T is larger. Particularly, in the annealed random landscape (Fig. 8(d)), individual TA MSDs converge to the MSD, Eq. (20) (dashed line), when T exceeds the homogenization time $\tau_c \approx 10^4$.

We analyze the trajectory-to-trajectory heterogeneity in terms of the ergodicity breaking (EB) parameter [5, 13, 14, 71, 72]

$$\text{EB}(\Delta, T) = \frac{\left\langle \left[\overline{\delta^2(\Delta, T)} \right]^2 \right\rangle - \left\langle \overline{\delta^2(\Delta, T)} \right\rangle^2}{\left\langle \overline{\delta^2(\Delta, T)} \right\rangle^2}. \quad (36)$$

In Fig. 8(e), we evaluate EB as a function of T for various values of D_{env} . The EB parameter monotonically decreases as D_{env} increases, suggesting that the annealing environment indeed tends to reduce the particle-to-particle heterogeneity, as discussed above. Notably, EB decays with two distinct power-law scalings: That is, a phenomenological power-law with an exponent less than unity for $t < \tau_c$ and the typical power-law T^{-1} for Gaussian diffusion after homogenization [13]. The first, anomalous regime is attributed to the spatiotemporally heterogeneous diffusion in the annealed random geometries. The strongest heterogeneity occurs in the quenched case, for which the power-exponent is smallest (≈ 0.45). As the annealing rate increases, the heterogeneous effect is weakened and, accordingly, the power-law exponent becomes larger. Beyond the homogenization timescale, the EB parameter converges to the universal relation $\text{EB} \sim T^{-1}$ satisfied by typical homogeneous ergodic diffusion processes, such as Brownian motion or the fractional Langevin equation model [5, 13, 14, 71, 72].

We estimate the crossover time at which the EB parameter starts to decay as $\simeq T^{-1}$. Because T^{-1} is the expected asymptotic scaling, we first define a threshold exponent θ_{EB} in the power-law scaling of the EB parameter $T^{-\theta_{\text{EB}}}$ and find the instant when the slope of the EB parameter, for the first time, becomes θ_{EB} . For two threshold exponents $\theta_{\text{EB}} = 0.95$ and $= 0.98$, we estimate the crossover timescales (symbols) for various values of the annealing rate [Fig. 8(f)]. The data are compared to the behavior of the homogenization time τ_c [Eq. (35), $\sqrt{N_H} = 100$] shown in Fig. 5(b). Excellent agreement between the two quantities is found, demonstrating that the convergence to ergodicity at long times is intimately related to the homogenization process.

V. DISCUSSION AND CONCLUSIONS

We here conceived an annealed extreme landscape model and performed a comprehensive computational and theoretical investigation on the non-Gaussian properties of a particle diffusing on this annealed heteroge-

neous environment. The main focus of this study is to characterize Fickian yet non-Gaussian diffusion in an annealed heterogeneous environment, with particular emphasis on how it relates to the annealing rate of the system and its convergence to homogeneous diffusion.

The four key findings of our study are as follows:

(1) Fickian diffusion is universal, regardless of the system's annealing rate, provided that the initial condition is stationary. We theoretically obtained the Fickian diffusion relation, $\langle \Delta x(t)^2 \rangle \approx 2 \langle D_S \rangle t$, which successfully explained the MSDs computed from the simulations. In this relation, the system's annealing increases the mean sampled diffusivity, $\langle D_S \rangle$, by assisting particles to escape from regions of slow diffusivity.

(2) The annealing of the system impacts the non-Gaussianity. When the annealing is slow, the Van-Hove self-correlation function is highly non-Gaussian, showing a pronounced peak around $\Delta x = 0$, as particles spend more time in regions of low diffusivity. When the annealing is faster, particles readily escape from slow diffusivity regions, resulting in a reduced peak around $\Delta x = 0$ in the Van-Hove self-correlation function. The Van-Hove self-correlation functions for varying D_{env} computed from the simulated trajectories are explained via the concept of superstatistics at short lag times and small Δx ($< r_c$).

(3) The annealing of the system reduces the homogenization time after which the initial non-Gaussian particle diffusion crosses over towards a Gaussian behavior. We found that this crossover emerges after the particle explores the space to a degree that the local random environment is sufficiently self-similar to the overall random landscape. As the particle samples the random environment faster in a rapidly annealing medium, the crossover timescales decrease monotonically with increasing D_{env} .

(4) Finally, the annealing of the random environment reduces the trajectory-trajectory heterogeneity. Before homogenization, each particle experiences a different surrounding environment. However, beyond the homogenization timescale, every particle effectively samples a sufficiently similar random environment. Consequently, the diffusion dynamics of different particles deviate negligibly from each other. This fact is corroborated by the occurrence of the inverse power-law scaling in the ergodicity breaking parameter, $EB(T) \sim T^{-1}$, at times beyond the homogenization time.

Let us now briefly discuss our findings with respect to previous studies on Fickian yet non-Gaussian diffusion phenomena. The main origin for Fickian yet non-Gaussian diffusion is the variability in the tracer diffusivity. The varying diffusivity is often due to the heterogeneous environment in which the tracer particles are embedded. Examples include the dynamics of beads diffusing along lipid tubes [23] or in polymer networks [21, 23, 25], and the motion of tracers in crowded [5, 24, 48] or disordered media [27]. As tracer particles explore such environments, their diffusivity fluctuates spatiotemporally. This gives rise to a varying diffusivity characterized by a diffusivity distri-

bution $\psi(D)$ [21, 23, 28, 30], which in turn produces a non-Gaussian van-Hove self-correlation function, as discussed in Sec. III B.

In most theoretical studies, the variability of the diffusivity is typically modeled as a stochastic process, such as the square of the Ornstein-Uhlenbeck process [28, 30, 73–76], a barometric formula-like scenario [31] the Feller process [32, 34], or switching diffusivity models [22, 77–79]. These studies commonly demonstrate that the particle diffusion in complex media leads to transient non-Gaussian diffusion over short timescales, which eventually crosses over to Gaussian diffusion beyond a characteristic correlation time, as predicted by the central limit theorem. Additionally, Fickian diffusion dynamics $\langle \Delta x^2(t) \rangle \propto t$ is observed when the initial ensemble is stationary. The Fickian yet non-Gaussian diffusion observed in an annealed extreme landscape in this study is in line with these previous findings. However, we stress that the previous theoretical models that assume a random time-dependent diffusivity do not fully account for the geometry and dynamics of the environment. In contrast, our annealed extreme landscape model is based on a specific realization of the geometry, represented by the local diffusivity field $D_L(\mathbf{r}, t)$, which also incorporates the environmental dynamics controlled by the annealing parameter D_{env} . In this setting, beyond the conventional discussions about a non-Gaussian van-Hove self correlation function or the scaling of the MSDs, we succeeded in relating the crossover timescale (i.e., the homogenization time) to the energy landscape and the annealing dynamics of the environment. Moreover, the dependence of the particle mean sampled diffusivity, $\langle D_S \rangle$, on the environmental annealing is a finding that has not been considered or predicted in previous random diffusivity models [32, 34, 73, 74].

To conclude, a thorough understanding of a medium's energy landscape the diffusive dynamics of a particle exploring the landscape are crucial to accurately quantify heterogeneities in the particle diffusion, such as non-Gaussianity and ergodicity breaking. Our study offers theoretical insights into how these factors are linked to the key timescales governing particle diffusion and demonstrates that the Fickian yet non-Gaussian diffusion indeed emerges in an annealed heterogeneous media. We propose several directions for future work related to our current study. Recently, fluctuating diffusivity models have been studied on the topics of diffusion-limited reactions and first-passage dynamics [32, 73, 74, 79–81]. As discussed, above, these models do not account for annealing-dependent mean sampled diffusivity and typically assume an *immobile* reactant target, which conflicts the assumptions of an annealing environment. A systematic understanding of diffusion-limited reactions in dynamic heterogeneous media, based on the explicit simulation of an annealed environment such as our annealed extreme landscape model and comparisons with conventional time-dependent diffusivity models, is needed. Furthermore, while our current model incorpo-

rates the environmental spatiotemporal variation via a two-dimensional lateral diffusion with local diffusivities $D_L(\mathbf{r})$, many real systems may have more complex geometry or higher dimension. Expanding the model to encompass these additional complexities is a challenge for future research.

Acknowledgments

This work was supported by the National Research Foundation (NRF) of Korea (grants RS-2023-00218927 & RS-2024-00343900). We also acknowledge funding from the German Science Foundation (DFG, grant ME 1535/13-2 and ME 1535/16-1).

Appendix A: Simulations details

Below we provide the details of the simulation algorithm, which involves five input variables: ω_{env} , r_c , L , δ , and T . These represent the annealing rate of the environment, the critical radius of an extreme basin, the size of the environment, the time resolution for perturbing the environment, and the total simulation time, respectively. The position of a particle at time t is denoted by $\mathbf{x}(t)$. The particle random walk is implemented using the Gillespie algorithm [82], and the auxiliary random field $U(\mathbf{r}, t)$ is updated at every time interval δ , with $\delta \leq 1$. The simulations output includes the time series $\mathbf{x}(t)$ of the particle and the sampled diffusivity $D_S(t)$.

Algorithm 1 Diffusion on an annealed landscape

Input: ω_{env} , r_c , L , δ , T
 $t \leftarrow 0$
 $\{U(\mathbf{r}, t)\} \leftarrow$ auxiliary random field [Eq. (3)]
 $\{V(\mathbf{r}, t)\} \leftarrow$ extreme landscape [Eq. (4)]
 $\mathbf{x}(t) \leftarrow$ initial position satisfying Eq. (11)
while $t < T$ **do**
 $\mathbf{x}(t+1) \leftarrow \mathbf{x}(t)$
 $\delta\text{sum} \leftarrow 0$
while $\delta\text{sum} < 1$ **do**
 $\eta\text{sum} \leftarrow 0$
while $\eta\text{sum} \leq \delta$ **do**
 $\omega \leftarrow \omega_0 \exp[V(\mathbf{x}, t + \delta\text{sum})]$
 $\eta \leftarrow -\log[1 - \text{unif}(0, 1)]/\omega$
 $\eta\text{sum} \leftarrow \eta\text{sum} + \eta$
if $\eta\text{sum} \leq \delta$ **then**
 $\mathbf{x}(t+1) \leftarrow$ one of its adjacent points
end if
end while
 $\{U(\mathbf{r}, t + \delta\text{sum} + \delta)\} \leftarrow$ disturbed $\{U(\mathbf{r}, t + \delta\text{sum})\}$
 $\{V(\mathbf{r}, t + \delta\text{sum} + \delta)\} \leftarrow$ extreme landscape
 $\delta\text{sum} \leftarrow \delta\text{sum} + \delta$
end while
 $t \leftarrow t + 1$
 $D_S(t) \leftarrow \pi r_c^2 \exp[V(\mathbf{x}(t), t)]$
end while
Output: $\{\mathbf{x}(t), D_S(t) \mid t < T\}$

Appendix B: PDFs from variable transformations

Here, we derive the PDFs $f_\omega(\omega)$ of the escape rate of a particle and of the sojourn time $f_\tau(\tau)$.

1. PDF of escape rates

The escape rate $\omega \in \mathbb{R}^+$ is defined by the transformation of the potential $V \in \mathbb{R}$ as in Eq. (7),

$$\omega = \omega_0 \exp(V). \quad (\text{B1})$$

The inverse transformation is given by

$$V = \log(\omega/\omega_0), \quad (\text{B2})$$

which involves the Jacobian $|dV/d\omega| = \omega^{-1}$. The PDF of ω is described as

$$\begin{aligned} f_\omega(\omega) &= \phi_V(V) \left| \frac{dV}{d\omega} \right| \\ &= \frac{\exp[V - V_0 - \exp(V - V_0)]}{\omega} \\ &= \frac{t_0}{4} \exp\left(-\frac{\omega t_0}{4}\right) \end{aligned} \quad (\text{B3})$$

with the unit simulation time $t_0 = 1$.

2. PDF of sojourn times

The sojourn time τ is defined by the transformation of the escape rate, as in Eq. (9),

$$\tau = \frac{1}{\omega + \omega_{\text{env}}}. \quad (\text{B4})$$

We note that τ satisfies $\tau \in (0, \omega_{\text{env}}^{-1})$ due to the constraint $\omega \in \mathbb{R}^+$. From the inverse transformation

$$\omega = \frac{1}{\tau} - \omega_{\text{env}} \quad (\text{B5})$$

we obtain the Jacobian $|d\omega/d\tau| = \tau^{-2}$. The PDF of τ is then described as

$$\begin{aligned} f_\tau(\tau) &= f_\omega(\omega) \left| \frac{d\omega}{d\tau} \right| \\ &= \frac{t_0}{4} \exp\left(-\frac{\omega t_0}{4}\right) \frac{1}{\tau^2} \\ &= \frac{t_0}{4\tau^2} \exp\left[-\frac{t_0}{4} \left(\frac{1}{\tau} - \omega_{\text{env}}\right)\right] \\ &= \frac{\tau_0 \exp(\omega_{\text{env}}\tau_0)}{\tau^2} \exp\left(-\frac{\tau_0}{\tau}\right), \end{aligned} \quad (\text{B6})$$

where $\tau_0 = t_0/4$. In the quenched limit $\omega_{\text{env}} = 0$, we recover the previous result obtained in the study of the quenched extreme landscape [44]. Note that both the quenched and annealed systems have the same power-law scaling $f_\tau(\tau) \sim \tau^{-2}$ for large τ .

Appendix C: MSD for a non-stationary diffusion trajectory

In the main text, we examined the MSD dynamics for stationary initial conditions, in which particles are initially located according to the stationary distribution (11). In Fig. A1(a), we plot the PDF of the initial sampled diffusivities $D_S(t=0)$ for $D_{\text{env}} = 0.5$ (black solid line), estimated from 1,000 simulated trajectories satisfying the stationary initial condition.

For a non-stationary initial condition, we selected the slowest 25% (250 trajectories) of the stationary ensemble, referred to as Q1, and the fastest 25%, referred to as Q4, based on their initial sampled diffusivities. This is graphically depicted in Fig. A1(a), in which the Q1 group is colored in blue and the Q4 group is colored in red.

In Fig. A1(b) and (c), we plot the MSDs for the non-stationary ensembles Q1 (blue) and Q4 (red), along with the theoretical MSD for the stationary state (black). The plots present the cases of (b) the quenched extreme landscape and of (c) the annealed extreme landscape ($D_{\text{env}} = 0.5$), respectively. At short times, the MSDs for the Q1 and Q4 groups exhibit Fickian diffusion with the mean diffusivities $\langle D_S \rangle_{\text{Q1}}$ and $\langle D_S \rangle_{\text{Q4}}$, averaged over the Q1 and Q4 populations, respectively. As a result, their MSDs are different from the theoretical MSD for the stationary ensemble.

As time increases beyond the homogenization time, the tracer particles reach the state of homogenization, and thus their MSDs (as well as the averaged sampled diffusivity) converge to $2\langle D_S \rangle t$, independent of the particle initial positions. At the cross-over timescale, a transient anomalous diffusion regime $\text{MSD} \sim t^\alpha$ ($\alpha \neq 1$) emerges, bridging between the short and long-time Fickian diffusion regimes. We also note that as the particles reach homogenization faster with an increased value for D_{env} , i.e., the long-time linear scaling $\sim 2\langle D_S \rangle t$ is observed earlier for $D_{\text{env}} = 0.5$ than for $D_{\text{env}} = 0$.

Appendix D: Calculation of the superstatistical integral

1. Exact solution of the superstatistical integral and asymptotic limit

Given a diffusion constant D_{env} , Eq. (22) is expressed as follows (the normalization is omitted for convenience):

$$p(x_\Delta, \Delta) \propto \int_0^\infty dD \frac{\exp\left(-\frac{x_\Delta^2}{4D\Delta} - \frac{D}{D_0}\right)}{\sqrt{4\pi D\Delta}} \frac{1}{D + D_{\text{env}}}. \quad (\text{D1})$$

To evaluate this integral, we utilize the identity

$$\frac{1}{D + D_{\text{env}}} = \int_0^\infty du e^{-u(D + D_{\text{env}})}. \quad (\text{D2})$$

As both integrals are finite, we can safely switch the

position of the two integrals, which yields

$$\begin{aligned} p(x_\Delta, \Delta) &\propto \int_0^\infty du \int_0^\infty dD \frac{e^{-\frac{x_\Delta^2}{4D\Delta} - \frac{D}{D_0}}}{\sqrt{4\pi D\Delta}} e^{-u(D + D_{\text{env}})} \\ &\propto \int_0^\infty du e^{-uD_{\text{env}}} \int_0^\infty dD \frac{e^{-(u + \frac{1}{D_0})D}}{\sqrt{4\pi D\Delta}} \\ &\quad \times \exp\left(-\frac{x_\Delta^2}{4D\Delta}\right). \end{aligned} \quad (\text{D3})$$

From a change of variable $y = \sqrt{D}$, we obtain

$$\begin{aligned} p(x_\Delta, \Delta) &\propto \sqrt{\frac{1}{\pi\Delta}} \int_0^\infty du e^{-uD_{\text{env}}} \\ &\quad \times \int_0^\infty dy \exp\left(-\left(u + \frac{1}{D_0}\right)y^2\right) \\ &\quad \times \exp\left(-\frac{x_\Delta^2}{4\Delta y^2}\right) \\ &= \sqrt{\frac{1}{4\Delta}} \int_0^\infty du e^{-uD_{\text{env}}} \frac{1}{\sqrt{u + \frac{1}{D_0}}} \\ &\quad \times \exp\left(-2\sqrt{\left(u + \frac{1}{D_0}\right)\frac{x_\Delta^2}{4\Delta}}\right). \end{aligned} \quad (\text{D4})$$

The change of variables $z = \sqrt{u + 1/D_0}$ leads to the Gaussian integral

$$\begin{aligned} p(x_\Delta, \Delta) &\propto \sqrt{\frac{1}{\Delta}} \int_{D_0^{-1/2}}^\infty dz e^{-(z^2 - \frac{1}{D_0})D_{\text{env}}} e^{-z\sqrt{x_\Delta^2/\Delta}} \\ &= \sqrt{\frac{\pi}{4D_{\text{env}}\Delta}} \text{erfc}\left(\frac{|x_\Delta|}{2\sqrt{D_{\text{env}}\Delta}} + \sqrt{\frac{D_{\text{env}}}{D_0}}\right) \\ &\quad \times \exp\left(\frac{x_\Delta^2}{4D_{\text{env}}\Delta} + \frac{D_{\text{env}}}{D_0}\right). \end{aligned} \quad (\text{D5})$$

This is the exact solution for our superstatistical integral presented in Eq. (D1). We now explore the asymptotic behavior of the PDF $p(x_\Delta, \Delta)$. In the asymptotic limit $|x_\Delta|/[2\sqrt{D_{\text{env}}\Delta}] + \sqrt{D_{\text{env}}/D_0} \gg 1$, indicative for large x_Δ , large D_{env} , small D_{env} , or small Δ , we employ the approximation $\text{erfc}(y) \approx \exp(-y^2)/[y\sqrt{\pi}]$ for large y . This yields

$$\begin{aligned} p(x_\Delta, \Delta) &\propto \sqrt{\frac{1}{4D_{\text{env}}\Delta}} \exp\left(\frac{x_\Delta^2}{4D_{\text{env}}\Delta} + \frac{D_{\text{env}}}{D_0}\right) \\ &\quad \times \frac{\exp\left(-\left[\frac{|x_\Delta|}{2\sqrt{D_{\text{env}}\Delta}} + \sqrt{\frac{D_{\text{env}}}{D_0}}\right]^2\right)}{\frac{|x_\Delta|}{2\sqrt{D_{\text{env}}\Delta}} + \sqrt{\frac{D_{\text{env}}}{D_0}}} \\ &\propto \frac{\exp\left(-\frac{|x_\Delta|}{\sqrt{D_0\Delta}}\right)}{|x_\Delta| + 2\sqrt{D_{\text{env}}\Delta}\sqrt{\frac{D_{\text{env}}}{D_0}}}. \end{aligned} \quad (\text{D6})$$

We display this analytical solution in Fig. A2 and compare it with the target PDF from Eq. (D1). The target

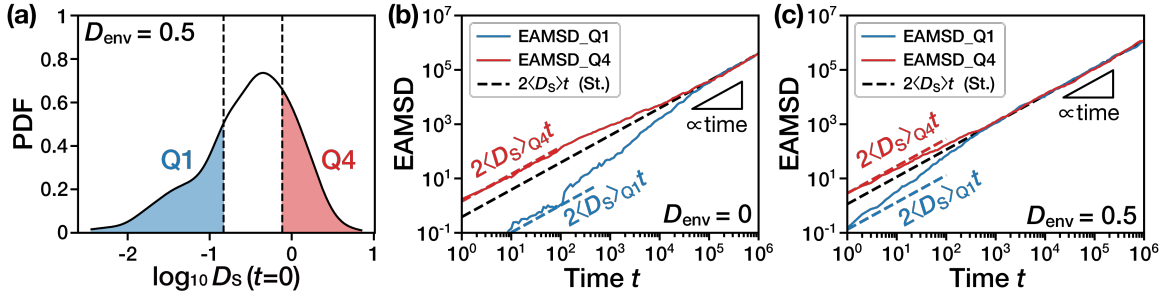


FIG. A1: **MSD for a non-stationary ensemble.** (a) Sampled diffusivity distribution for $D_{\text{env}} = 0.5$, estimated using the simulated trajectories with stationary initial condition (black) and non-stationary populations chosen from the slowest 25% (Q1, blue) and the fastest 25% (Q4, red). (b) and (c) MSDs for non-stationary ensembles Q1 and Q4 (blue) and Q4 (red) at (b) $D_{\text{env}} = 0$ and at (c) $D_{\text{env}} = 0.5$. At short times, the MSDs for the Q1 and Q4 groups exhibit the Fickian law $2\langle D_S \rangle_{Q1} t$ and $2\langle D_S \rangle_{Q4} t$, respectively. At long times, both MSDs converge to $2\langle D_S \rangle t$.

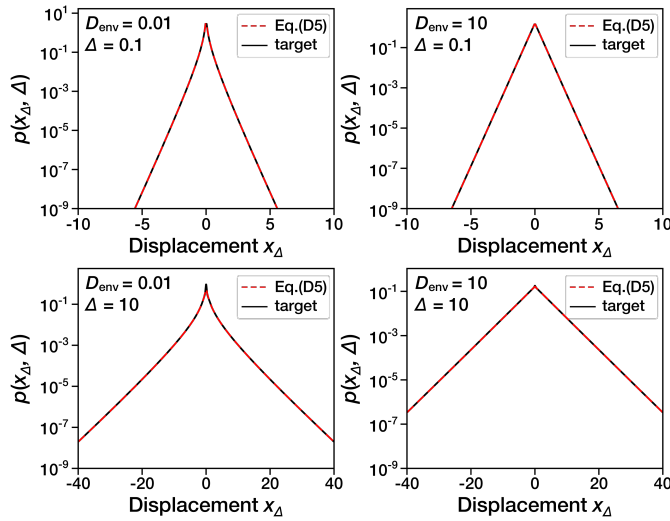


FIG. A2: **Displacement PDFs for superstatistical integration, Eq. (D1).** Black solid lines represent the numerical evaluation of Eq. (D1), and red dashed lines show Eqs. (D5). The red dashed lines perfectly match the black solid lines.

PDFs, shown as black solid lines, were derived by numerically superimposing Gaussian PDFs weighted by $\psi(D)$. The perfect alignment of these plots across various D_{env} and Δ values verifies our analytical solution.

2. Approximation of a superstatistical integral with Gaussian PDFs

Although we obtained the exact solution for $p(x_\Delta, \Delta)$, it is often nontrivial to calculate such kinds of superstatistical integrals. In this Subsection, we introduce a method for approximating superstatistical integrals. The basic idea of our approach is quite similar to the saddle point approximation [45]. We consider the following in-

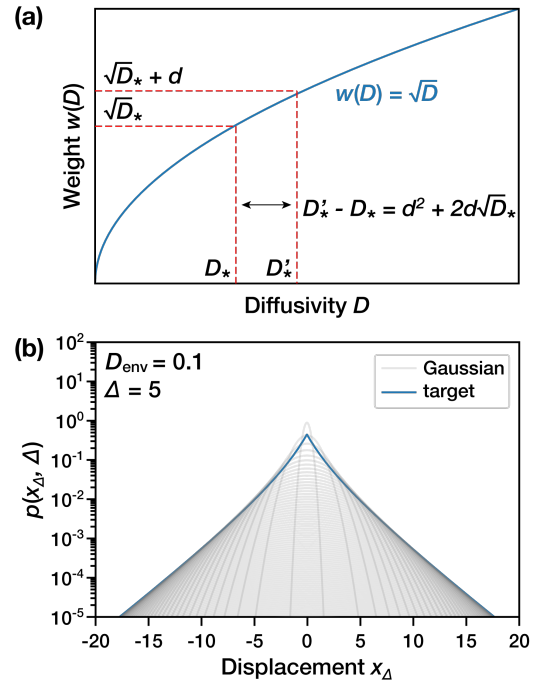


FIG. A3: **Approximation of a superstatistical integral with Gaussian PDFs.** (a) Characteristic width of Gaussian PDF vs. diffusivity D . (b) Schematic illustration of the approximation for the displacement PDF $p(x_\Delta, \Delta)$. Gray solid lines are Gaussian PDFs with diffusivity D , multiplied by the effective weight $\psi(D)\sqrt{D}$. Blue solid line: numerically evaluated superstatistical integral (D1).

tegral

$$p(x_\Delta, \Delta) = \int_0^\infty dD \psi(D) G(x_\Delta, \Delta|D). \quad (\text{D7})$$

This integral implies that we superpose Gaussian PDFs $G(x_\Delta, \Delta|D)$ for a specific D , weighted by $\psi(D)$, as D varies linearly from 0 to infinity. We define the characteristic width of a Gaussian PDF $(4\pi D \Delta)^{-1/2} \exp(-x_\Delta^2/[4D \Delta])$ as $w(D) = \sqrt{D}$. For a

given $D = D_*$, consider its characteristic width $w(D_*) = \sqrt{D_*}$ and some infinitesimally small interval d just above $\sqrt{D_*}$, as illustrated in Fig. A3(a). The length of the diffusivity domain that corresponds to characteristic widths within the range $w(D) \in [\sqrt{D_*}, \sqrt{D_*} + d]$ is given by $D'_* - D_* = d^2 + 2d\sqrt{D_*}$. Consequently, for Gaussian PDFs with widths $w(D)$ in the range $[\sqrt{D}, \sqrt{D} + d]$, the effective weight can be approximated as

$$\psi(D)(d^2 + 2d\sqrt{D}) \approx \psi(D)(2d\sqrt{D}) \propto \psi(D)\sqrt{D}. \quad (\text{D8})$$

We now define $D_{\max}(x)$ as the diffusivity that maximizes the contribution at $x_\Delta = x$,

$$D_{\max}(x) = \operatorname{argmax}_D \left\{ \psi(D)G(x_\Delta = x, \Delta|D)\sqrt{D} \right\}. \quad (\text{D9})$$

Since the value of a Gaussian PDF $G(x_\Delta, \Delta|D)$ at a fixed x_Δ varies significantly with changes in its parameter D , the contribution from a Gaussian PDF with $D_{\max}(x_\Delta)$, represented as $\psi(D_{\max}(x_\Delta))G(x_\Delta, \Delta|D_{\max}(x_\Delta))\sqrt{D_{\max}(x_\Delta)}$, dominates the value of $p(x_\Delta, \Delta)$. Consequently, we can approximate $p(x_\Delta, \Delta)$ as

$$p(x_\Delta = x, \Delta) \approx \mathcal{N} \psi[D_{\max}(x)]G[x, \Delta|D_{\max}(x)] \times \sqrt{D_{\max}(x)}, \quad (\text{D10})$$

where \mathcal{N} is a normalization factor.

We graphically illustrate the approximation process described above in Fig. A3(b). The target displacement PDF (22) for $D_{\text{env}} = 0.1$ is shown as the blue solid line. This PDF is juxtaposed with the multiple Gaussian PDFs $\psi(D)G(x_\Delta, \Delta|D)\sqrt{D}$, each corresponding to different D values, depicted as grey solid lines. Essentially, the approximation in Eq. (D10) involves deriving the outer envelope of these multiple Gaussians.

By inserting the weight function $\psi(D) \propto \exp(-D/D_0)/(D + D_{\text{env}})$, we find

$$p(x_\Delta, \Delta) \approx \frac{\mathcal{N}' \exp \left[-\frac{x_\Delta^2}{4D_{\max}(x_\Delta)\Delta} - \frac{D_{\max}(x_\Delta)}{D_0} \right]}{\sqrt{\Delta} (D_{\max}(x_\Delta) + D_{\text{env}})}, \quad (\text{D11})$$

where \mathcal{N}' is a normalization factor and

$$D_{\max}(x_\Delta) = -\frac{1}{3}(D_{\text{env}} + D_0) + \frac{[\beta + (4\alpha^3 + \beta^2)^{1/2}]^{1/3}}{12 \cdot 2^{1/3}} - \frac{\alpha}{6 \cdot 2^{2/3} [\beta + (4\alpha^3 + \beta^2)^{1/2}]^{1/3}} \quad (\text{D12})$$

with

$$\begin{aligned} \alpha &= -16(D_{\text{env}} + D_0)^2 - \frac{12}{\Delta} D_0 x_\Delta^2 \\ \beta &= -128D_{\text{env}}^3 - 384D_0 D_{\text{env}}^2 - 384D_0^2 D_{\text{env}} - 128D_0^3 \\ &\quad + \frac{288}{\Delta} D_0 D_{\text{env}} x_\Delta^2 - \frac{144}{\Delta} D_0^2 x_\Delta^2. \end{aligned} \quad (\text{D13})$$

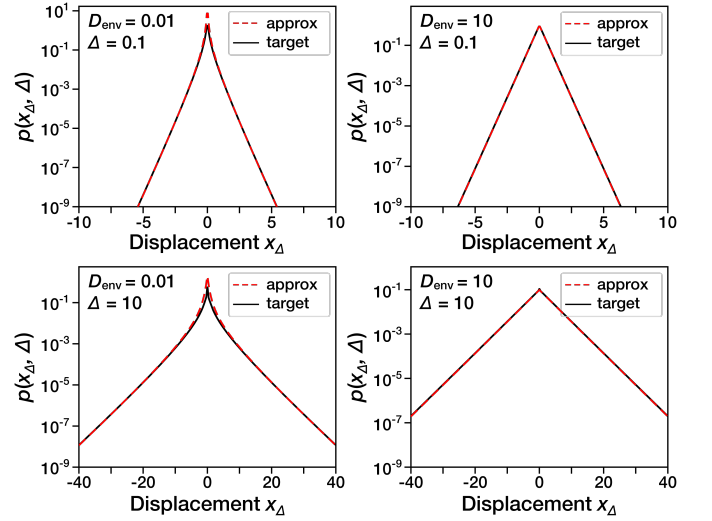


FIG. A4: **Displacement PDFs for superstatistical integral (D1) with approximation (D11).** Black solid lines are obtained from the numerical evaluation of Eq. (D1), and red dashed lines are plotted using Eq. (D11). The red dashed lines show a slight deviation from the target PDF for small $D_{\text{env}} (= 0.01)$, while they perfectly match the target PDF for large $D_{\text{env}} (= 10)$.

From Eq. (D11), one can derive the asymptotic forms

$$p(x_\Delta, \Delta) \approx \begin{cases} \frac{2\mathcal{N}'}{\sqrt{D_0|x_\Delta|}} \exp\left(-\frac{|x_\Delta|}{\sqrt{D_0\Delta}}\right), & \frac{x_\Delta^2}{\Delta} \gg D_0, D_{\text{env}} \\ \frac{\mathcal{N}'}{D_{\text{env}}\sqrt{\Delta}} \exp\left(-\frac{|x_\Delta|}{\sqrt{D_0\Delta}}\right), & \text{large } D_{\text{env}}, \end{cases} \quad (\text{D14})$$

which are the same as Eq. (25) and (26).

We compare our result (D11) with the target PDF in Fig. A4. For small $D_{\text{env}} (= 0.01)$, the tails at $x_\Delta^2/\Delta \gg D_{\text{env}}$ perfectly overlap with the target PDF (black). For large $D_{\text{env}} (= 10)$, the tails are well matched for all cases, while the peaks deviate somewhat from the target PDF for small D_{env} .

Appendix E: Non-Gaussianity parameter for finite-length trajectories

The non-Gaussianity parameter (NGP) for a one-dimensional (1D), centered random variable X is typically defined as

$$\begin{aligned} \text{NGP}(X) &= \frac{1}{3} \times \text{Kurt}[X] - 1 \\ &= \frac{1}{3} \times \frac{\mathbb{E}[X^4]}{\mathbb{E}[X^2]^2} - 1. \end{aligned} \quad (\text{E1})$$

For Gaussian-distributed independent and identically distributed (i.i.d.) random samples $X_i \sim \mathcal{N}(0, \sigma^2)$, the NGP is zero because the kurtosis of a Gaussian PDF is three. However, when dealing with a finite realization

$\{X_i\}_{i=1}^N$ with ($N < \infty$) of i.i.d. random samples, these samples do not follow an ideal Gaussian PDF due to the presence of a cutoff. According to extreme value statistics [83], the cutoff is $\mathbb{E}[\max X|N] = \sigma\sqrt{2\log N}$. The samples instead follow a truncated normal distribution defined on $X \in [-\sigma\sqrt{2\log N}, \sigma\sqrt{2\log N}]$, resulting in a negative NGP.

For a finite number of random samples, we propose the modified NGP (mNGP) in the form

$$\widehat{\text{NGP}}(X; N) = \text{NGP}(X) - \text{NGP}_0. \quad (\text{E2})$$

Here, NGP_0 refers to NGP for the random variable $\xi_N^{\text{tn}} \in [-\sqrt{2\log N}, \sqrt{2\log N}]$ of a truncated standard normal PDF, where N is the number of independent samples. If NGP for the random variable X is very similar to that of ξ_N^{tn} , the mNGP of X becomes almost zero, and one can infer that the random samples X are Gaussian-distributed. Here, we used the truncated *standard* normal PDF because a truncated normal PDF with σ , N , and the domain $[-\sigma\sqrt{2\log N}, \sigma\sqrt{2\log N}]$ exhibits the same NGP values independent of σ , solely depending on N . In our work, the second and fourth moments of the truncated normal PDF, which are necessary to calculate NGP, are computed using the SciPy module in Python [84].

For a trajectory dataset with the observation time T and particle number N_{par} , mNGP for the displacement of x_Δ is defined as

$$\widehat{\text{NGP}}(x_\Delta; \Delta, T, N_{\text{par}}) = \text{NGP}(x_\Delta) - \text{NGP}_0. \quad (\text{E3})$$

Here, the NGP_0 refers to the truncated normal random variables with $N_{\text{par}}T/\Delta$ independent displacement samples.

In Fig. A5, we test the validity of mNGP with stochastic simulations. We simulated Brownian trajectories for which the unit-time displacement $x(t+1) - x(t)$ was updated according to a Gaussian PDF $\mathcal{N}(0, 2D)$. The simulations were performed with $D = 0.5$, $T = 50000$, and $N_{\text{par}} = 500$. For a given lag time Δ , the variance of x_Δ satisfies $\langle x_\Delta^2 \rangle = \Delta$.

First, Fig. A5(a) presents the maximal displacement among $\{x(t + \Delta) - x(t)\}$ from a single trajectory for a given Δ . The gray lines are results from individual trajectories and the red solid line shows their average value for the given Δ . It is confirmed that the averaged maximal displacement (red) is in excellent agreement with the theoretical behavior $\sim \sigma\sqrt{2\log(T/\Delta)}$ (lower dashed line) expected from extreme value statistics. We also observe that the theoretical maximal displacement for N_{par} trajectories (upper dashed line) explains very well the observed global maximal displacement across all lag times investigated.

Second, we plot in Fig. A5(b) the conventional NGP (E1) for individual trajectories (gray) as a function of Δ . Their median values are depicted as the red solid line, which agrees nicely with the theoretical curve for the NGP of a truncated normal PDF with $T = 50000$ and

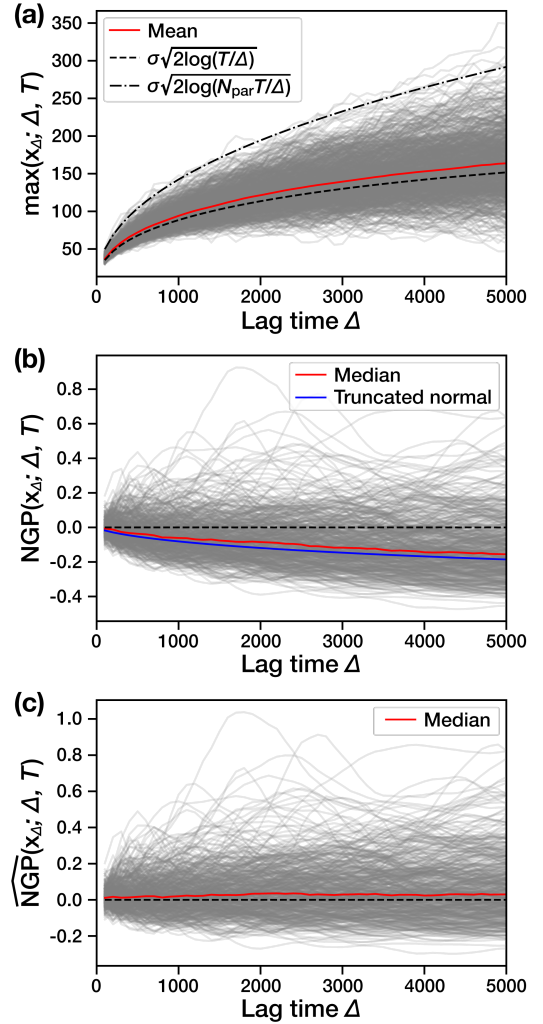


FIG. A5: **Cutoff displacement and non-Gaussianity parameter of finite-length Brownian trajectories for $D = 0.5$, $N_{\text{par}} = 500$, and $T = 50000$.** (a) Maximal displacement as function of lag time Δ . The gray line represents the observed maximal displacement from individual simulated trajectories, and their average is depicted by the red solid line. Additionally, two theoretical values are depicted: (i) The upper dashed line is the theoretical global maximum displacement for N_{par} trajectories. (ii) The lower dashed line indicates the theoretical maximum displacement for a single trajectory. (b) The conventional NGPs for individual trajectories (gray), their median value (red), and the theoretical NGP for a truncated normal PDF, $\text{NGP}(\xi_{N_{\text{par}}}^{\text{tn}})$ (blue). The black dashed line denotes the zero value. (c) mNGPs for individual trajectories (gray) and their median value (red), the black dashed line shows the zero value.

$N_{\text{par}} = 1$ (blue). Since NGP is calculated from individual trajectories in the plot, the theoretical curve is plotted with $N_{\text{par}} = 1$. Note that although we simulated a Gaussian process, the finite Brownian trajectories result in a negative NGP, as expected from our discussion.

Third, in Fig. A5(c), we show mNGP for the simulated trajectories. mNGP for individual trajectories is shown

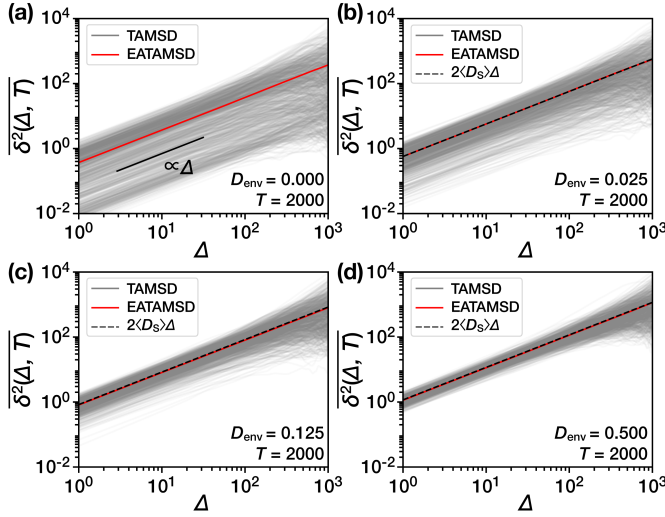


FIG. A6: **TAMSD for short observation time** $T = 2 \times 10^3$. In all panels, TAMSDs from individual tracers (gray lines) are plotted together with their average, i.e., the EATAMSD (black thick line). Eq. (20) is represented by the dashed line.

in gray, while their median value is depicted in red. We

demonstrate that, in contrast to the conventional NGP, mNGP fluctuates around zero, indicating that it provides a more reliable measure for Gaussianity as compared to the conventional NGP.

Appendix F: Time-averaged mean squared displacement

In Fig. A6 we show the TAMSD for short observation time, $T = 2000$ (compare with Fig. 8), much shorter than the homogenization times ($10^4 \dots 10^5$) of the extreme landscapes we investigated in the main text. The scatter in the amplitudes of the TAMSD from their average is substantial as compared to the results in Fig. 8 with $T = 2 \times 10^6$.

Figure A7 shows the TAMSD as a function of the observation time T in the quenched case, $D_{\text{env}} = 0$, for $L = 1024$. We compare the EATAMSD for this case (red line) with the EATAMSD for $L = 512$ (blue line). The value of the EATAMSD becomes smaller when a particle diffuses in a larger ($L = 1024$) environment, as anticipated in the discussion in Sec. IV B. As the size of the environment L becomes larger, deeper traps $V(\mathbf{r})$ appear.

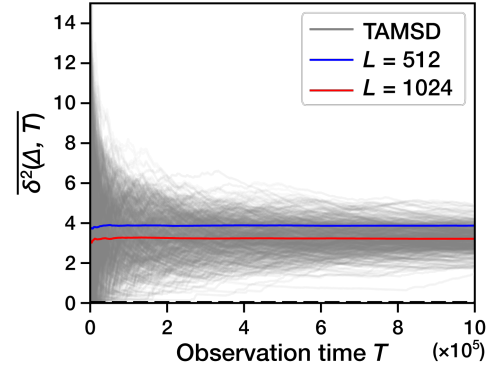


FIG. A7: **TAMSD as function of observation time** T for $D_{\text{env}} = 0$. Gray solid lines are TAMSDs of tracers diffusing on a quenched environment with $L = 1024$, the red line represents their EATAMSD. For comparison, the EATAMSD for $L = 512$ is also shown (blue line).

-
- [1] A. D. Riggs, S. Bourgeois, and M. Cohn, *J. Mol. Biol.* **53**, 401 (1970).
 - [2] O. G. Berg, R. B. Winter, and P. H. Von Hippel, *Biochemistry* **20**, 6929 (1981).
 - [3] S. Park, O.-c. Lee, X. Durang, J.-H. Jeon, et al., *J. Korean Phys. Soc.* **78**, 408 (2021).
 - [4] O. Pulkkinen and R. Metzler, *Phys. Rev. Lett.* **110**, 198101 (2013).
 - [5] J.-H. Jeon, M. Javanainen, H. Martinez-Seara, R. Metzler, and I. Vattulainen, *Phys. Rev. X* **6**, 021006 (2016).
 - [6] D. Y. Vargas, A. Raj, S. A. Marras, F. R. Kramer, and S. Tyagi, *Proc. Natl. Acad. Sci.* **102**, 17008 (2005).
 - [7] M. S. Song, H. C. Moon, J.-H. Jeon, and H. Y. Park, *Nat. Commun.* **9**, 1 (2018).
 - [8] T. J. Lampo, S. Stylianidou, M. P. Backlund, P. A. Wiggins, and A. J. Spakowitz, *Biophys. J.* **112**, 532 (2017).
 - [9] C. Bechinger, R. Di Leonardo, H. Löwen, C. Reichhardt, G. Volpe, and G. Volpe, *Rev. Mod. Phys.* **88**, 045006 (2016).
 - [10] A. Cherstvy, O. Nagel, C. Beta, and R. Metzler, *Phys. Chem. Chem. Phys.* **20**, 23034 (2018).
 - [11] R. Großmann, L. S. Bort, T. Moldenhawer, M. Stange, S. S. Panah, R. Metzler, and C. Bets, *Phys. Rev. Lett.* **132**, 088301 (2024).
 - [12] F. Höfling and T. Franosch, *Rep. Prog. Phys.* **76**, 046602 (2013).
 - [13] R. Metzler, J.-H. Jeon, A. G. Cherstvy, and E. Barkai, *Phys. Chem. Chem. Phys.* **16**, 24128 (2014).
 - [14] D. Krapf and R. Metzler, *Phys. Today* **72(9)**, 48 (2019).
 - [15] G. Muñoz-Gil, G. Volpe, M. A. Garcia-March, E. Aghion, A. Argun, C. B. Hong, T. Bland, S. Bo, J. A. Conejero, N. Firbas, et al., *Nat. Commun.* **12**, 1 (2021).
 - [16] M. Weiss, M. Elsner, F. Kartberg, and T. Nilsson, *Biophys. J.* **87**, 3518 (2004).
 - [17] A. Caspi, R. Granek, and M. Elbaum, *Phys. Rev. Lett.* **85**, 5655 (2000).
 - [18] I. Goychuk, *Phys. Rev. E* **80**, 046125 (2009).
 - [19] I. Goychuk, *Adv. Chem. Phys.* **150**, 187 (2012).
 - [20] H. Scher and E. W. Montroll, *Phys. Rev. B* **12**, 2455 (1975).
 - [21] B. Wang, J. Kuo, S. C. Bae, and S. Granick, *Nat. Mater.* **11**, 481 (2012).

- [22] A. Sabri, X. Xu, D. Krapf, and M. Weiss, *Phys. Rev. Lett.* **125**, 058101 (2020).
- [23] B. Wang, S. M. Anthony, S. C. Bae, and S. Granick, *Proc. Natl. Acad. Sci.* **106**, 15160 (2009).
- [24] S. K. Ghosh, A. G. Cherstvy, and R. Metzler, *Phys. Chem. Chem. Phys.* **17**, 1847 (2015).
- [25] C. Xue, X. Zheng, K. Chen, Y. Tian, and G. Hu, *J. Phys. Chem. Lett.* **7**, 514 (2016).
- [26] A. G. Cherstvy, S. Thapa, C. E. Wagner, and R. Metzler, *Soft Matter* **15**, 2526 (2019).
- [27] I. Chakraborty and Y. Roichman, *Phys. Rev. Lett.* **2**, 022020 (2020).
- [28] A. V. Chechkin, F. Seno, R. Metzler, and I. M. Sokolov, *Phys. Rev. X* **7**, 021002 (2017).
- [29] J. M. Miotto, S. Pigolotti, A. V. Chechkin, and S. Roldán-Vargas, *Phys. Rev. X* **11**, 031002 (2021).
- [30] V. Sposini, A. V. Chechkin, F. Seno, G. Pagnini, and R. Metzler, *New J. Phys.* **20**, 043044 (2018).
- [31] M. V. Chubynsky and G. W. Slater, *Phys. Rev. Lett.* **113**, 098302 (2014).
- [32] Y. Lanoiselée, N. Moutal, and D. S. Grebenkov, *Nat. Commun.* **9**, 1 (2018).
- [33] S. Thapa, M. A. Lomholt, J. Krog, A. G. Cherstvy, and R. Metzler, *Phys. Chem. Chem. Phys.* **20**, 29018 (2018).
- [34] Y. Lanoiselée and D. S. Grebenkov, *J. Phys. A: Math. Theor.* **51**, 145602 (2018).
- [35] T. Uneyama, T. Miyaguchi, and T. Akimoto, *Phys. Rev. E* **92**, 032140 (2015).
- [36] E. Yamamoto, T. Akimoto, A. Mitsutake, and R. Metzler, *Phys. Rev. Lett.* **126**, 128101 (2021).
- [37] T. Miyaguchi, *Phys. Rev. E* **96**, 042501 (2017).
- [38] K. Kamagata, E. Mano, K. Ouchi, S. Kanbayashi, and R. C. Johnson, *J. Mol. Biol.* **430**, 655 (2018).
- [39] C. Beck and E. G. Cohen, *Physica A* **322**, 267 (2003).
- [40] S. Thapa, S. Park, Y. Kim, J.-H. Jeon, R. Metzler, and M. A. Lomholt, *J. Phys. A: Math. Theor.* **55**, 194003 (2022).
- [41] J.-P. Bouchaud and A. Georges, *Phys. Rep.* **195**, 127 (1990).
- [42] S. Burov, *Phys. Rev. E* **96**, 050103(R) (2017).
- [43] E. B. Postnikov, A. Chechkin, and I. M. Sokolov, *New J. Phys.* **22**, 063046 (2020).
- [44] L. Luo and M. Yi, *Phys. Rev. E* **97**, 042122 (2018).
- [45] L. Luo and M. Yi, *Phys. Rev. E* **100**, 042136 (2019).
- [46] R. Metzler, J.-H. Jeon, and A. Cherstvy, *Biochim. Biophys. Acta - Biomembr.* **1858**, 2451 (2016).
- [47] A. V. Weigel, B. Simon, M. M. Tamkun, and D. Krapf, *Proc. Natl. Acad. Sci.* **108**, 6438 (2011).
- [48] W. He, H. Song, Y. Su, L. Geng, B. J. Ackerson, H. B. Peng, and P. Tong, *Nat. Commun.* **7**, 11701 (2016).
- [49] M. Di Pierro, D. A. Potoyan, P. G. Wolynes, and J. N. Onuchic, *Proc. Natl. Acad. Sci.* **115**, 7753 (2018).
- [50] D. Sung, C. Lim, M. Takagi, C. Jung, H. Lee, D. H. Cho, J.-Y. Shin, K. Ahn, J. Hwang, D. Nam, et al., *Proc. Natl. Acad. Sci.* **118**, e2109921118 (2021).
- [51] D. Saintillan, M. J. Shelley, and A. Zidovska, *Proc. Natl. Acad. Sci.* **115**, 11442 (2018).
- [52] A. Mahajan, W. Yan, A. Zidovska, D. Saintillan, and M. J. Shelley, *bioRxiv* (2022).
- [53] A. Zidovska, D. A. Weitz, and T. J. Mitchison, *Proc. Natl. Acad. Sci.* **110**, 15555 (2013).
- [54] E. J. Banigan and L. A. Mirny, *Curr. Opin. Cell Biol.* **64**, 124 (2020).
- [55] Y. Kim, Z. Shi, H. Zhang, I. J. Finkelstein, and H. Yu, *Science* **366**, 1345 (2019).
- [56] A. S. Hansen, C. Cattoglio, X. Darzacq, and R. Tjian, *Nucleus* **9**, 20 (2018).
- [57] S. Joo, X. Durang, O.-c. Lee, and J.-H. Jeon, *Soft Matter* **16**, 9188 (2020).
- [58] S. Thapa, N. Lukat, C. Selhuber-Unkel, A. G. Cherstvy, and R. Metzler, *J. Chem. Phys.* **150**, 144901 (2019).
- [59] J. F. Reverey, J.-H. Jeon, H. Bao, M. Leippe, R. Metzler, and C. Selhuber-Unkel, *Sci. Rep.* **5**, 1 (2015).
- [60] M. Guo, A. J. Ehrlicher, M. H. Jensen, M. Renz, J. R. Moore, R. D. Goldman, J. Lippincott-Schwartz, F. C. Mackintosh, and D. A. Weitz, *Cell* **158**, 822 (2014).
- [61] T. Sungkaworn, M.-L. Jobin, K. Burnecki, A. Weron, M. J. Lohse, and D. Calebiro, *Nature* **550**, 543 (2017).
- [62] S. Sadegh, J. L. Higgins, P. C. Mannion, M. M. Tamkun, and D. Krapf, *Phys. Rev. X* **7**, 011031 (2017).
- [63] A. S. Moore, Y. C. Wong, C. L. Simpson, and E. L. Holzbaur, *Nat. Commun.* **7**, 1 (2016).
- [64] P. Massignan, C. Manzo, J. A. Torreno-Pina, M. F. García-Parajo, M. Lewenstein, and G. Lapeyre Jr, *Phys. Rev. Lett.* **112**, 150603 (2014).
- [65] M. Abramowitz and I. A. Stegun, *Handbook of Mathematical Functions with Formulas, Graphs, and Mathematical Tables*, vol. 55 (US Government Printing Office, 1964).
- [66] *Supplementary material: Movies for simulated diffusion dynamics in an annealed extreme landscape*, https://github.com/sgp105/Extreme_Movies.git (2025).
- [67] E. Barkai, Y. Garini, and R. Metzler, *Phys. Today* **65(8)**, 29 (2012).
- [68] W. Wang, Y. Liang, A. V. Chechkin, and R. Metzler, *Phys. Rev. E* (2025), in press.
- [69] M. Biroli, F. Mori, and S. N. Majumdar, *J. Phys. A: Math. Theor.* **55**, 244001 (2022).
- [70] R. M. Corless, G. H. Gonnet, D. E. Hare, D. J. Jeffrey, and D. E. Knuth, *Adv. Comput. Math.* **5**, 329 (1996).
- [71] Y. He, S. Burov, R. Metzler, and E. Barkai, *Phys. Rev. Lett.* **101**, 058101 (2008).
- [72] W. Deng and E. Barkai, *Phys. Rev. E* **79**, 011112 (2009).
- [73] V. Sposini, S. Nampoothiri, A. Chechkin, E. Orlandini, F. Seno, and F. Baldovin, *Phys. Rev. E* **109**, 034120 (2024).
- [74] V. Sposini, S. Nampoothiri, A. Chechkin, E. Orlandini, F. Seno, and F. Baldovin, *Phys. Rev. Lett.* **132**, 117101 (2024).
- [75] R. Jain and K. L. Sebastian, *J. Phys. Chem. B* **120**, 9215 (2016).
- [76] N. Tyagi and B. J. Cherayil, *J. Phys. Chem. B* **121**, 7204 (2017).
- [77] T. Miyaguchi, T. Uneyama, and T. Akimoto, *Phys. Rev. E* **100**, 012116 (2019).
- [78] T. J. Doerries, A. V. Chechkin, and R. Metzler, *J. R. Soc. Interface* **19**, 20220233 (2022).
- [79] D. S. Grebenkov, *J. Phys. A: Math. Theor.* **52**, 174001 (2019).
- [80] V. Sposini, A. Chechkin, and R. Metzler, *J. Phys. A: Math. Theor.* **52**, 04LT01 (2018).
- [81] D. S. Grebenkov, V. Sposini, R. Metzler, G. Oshanin, and F. Seno, *J. Phys. A: Math. Theor.* **54**, 04LT01 (2021).
- [82] D. T. Gillespie, *J. Phys. Chem.* **81**, 2340 (1977).
- [83] E. J. Gumbel, *Statistics of extremes* (Columbia university press, 1958).
- [84] P. Virtanen, R. Gommers, T. E. Oliphant, M. Haberland, T. Reddy, D. Cournapeau, E. Burovski, P. Peter-

son, W. Weckesser, J. Bright, et al., *Nat. Methods* **17**, 261 (2020).